ARMY RESEARCH LABORATORY

Predicting Grain Growth in Nanocrystalline Materials: A Thermodynamic and Kinetic-Based Model Informed by High Temperature X-ray Diffraction Experiments

by Mark A Tschopp, Kris A Darling,
Mark A Atwater, Kiran N Solanki

ARL-TR-7107 October 2014

NOTICES

Disclaimers

Army Research Laboratory
Aberdeen Proving Ground, MD 21005-5069

ARL-TR-7107 **October 2014**

Predicting Grain Growth in Nanocrystalline Materials: A Thermodynamic and Kinetic-Based Model Informed by High Temperature X-ray Diffraction Experiments

Mark A Tschopp, Kris A Darling
Weapons and Materials Research Directorate

Mark A Atwater
Department of Applied Engineering, Safety & Technology
Millersville University

Kiran N Solanki
School for Engineering of Matter, Transport and Energy
Arizona State University

REPORT DOCUMENTATION PAGE

Form Approved
OMB No. 0704-0188

1. REPORT DATE *(DD-MM-YYYY)*
October 2014

2. REPORT TYPE
Final

3. DATES COVERED (From - To)
November 2012–October 2014

4. TITLE AND SUBTITLE
Predicting Grain Growth in Nanocrystalline Materials: A Thermodynamic and Kinetic-Based Model Informed by High Temperature X-ray Diffraction Experiments

5a. CONTRACT NUMBER

5b. GRANT NUMBER

5c. PROGRAM ELEMENT NUMBER

6. AUTHOR(S)
Mark A Tschopp, Kris A Darling, Mark A Atwater, Kiran N Solanki

5d. PROJECT NUMBER

5e. TASK NUMBER

5f. WORK UNIT NUMBER

7. PERFORMING ORGANIZATION NAME(S) AND ADDRESS(ES)
US Army Research Laboratory
ATTN: RDRL-WMM-F
Aberdeen Proving Ground, MD 21005

8. PERFORMING ORGANIZATION REPORT NUMBER
ARL-TR-7107

9. SPONSORING/MONITORING AGENCY NAME(S) AND ADDRESS(ES)

10. SPONSOR/MONITOR'S ACRONYM(S)

11. SPONSOR/MONITOR'S REPORT NUMBER(S)

12. DISTRIBUTION/AVAILABILITY STATEMENT
Approved for public release; distribution is unlimited.

13. SUPPLEMENTARY NOTES

14. ABSTRACT

Predicting grain growth in nanocrystalline materials requires modeling approaches that incorporate grain boundary thermodynamics and kinetics. In this work, a thermokinetic model for grain growth was applied to experimental X-ray diffraction measurements from nanocrystalline Fe–Zr in an effort 1) to understand the influence of thermodynamic, kinetic, and material parameters in the model; and 2) to extend the thermokinetic model by incorporating temperature dependence. The model performs well for the grain boundary saturated case in the nanocrystalline Fe–Zr system, where Zr segregate to the Fe grain boundaries and thermodynamically/kinetically reduce the driving force for grain growth. In this work, a sensitivity analysis of parameters (Monte Carlo global sensitivity analysis with 10,000 instantiations) identifies the important thermodynamic/kinetic parameters for the model. This model was then extended to include the change in these independent thermodynamic/kinetic parameters as a function of temperature and to model the effect of grain size distribution. The significance of this research is that the thermodynamic and kinetic contributions may be necessary to help explain grain growth in nanocrystalline materials and this extended model can be applied to understanding how grain size evolves with temperature in other nanocrystalline systems.

15. SUBJECT TERMS
thermokinetic model; grain growth; nanocrystalline materials; Fe–Zr; thermodynamics; kinetics; sensitivity analysis

16. SECURITY CLASSIFICATION OF:			17. LIMITATION OF ABSTRACT	18. NUMBER OF PAGES	19a. NAME OF RESPONSIBLE PERSON Mark A Tschopp
a. REPORT Unclassified	b. ABSTRACT Unclassified	c. THIS PAGE Unclassified	UU	79	19b. TELEPHONE NUMBER (*Include area code*) 410-306-0855

Standard Form 298 (Rev. 8/98)
Prescribed by ANSI Std. Z39.18

Contents

List of Figures

List of Tables

1. Introduction

The evolution of material microstructure during processing plays a commanding role in the physical properties and mechanisms in materials. Hence, establishing the processing-structure and structure-property relationships can help accelerate the design and development of new metals. Without such relationships, achieving meaningful advances becomes a highly empirical, hit-and-miss undertaking. Many materials already have a significant foundational understanding from decades of research, but emerging material classes such as nanocrystalline alloys are still not as well understood. Experimental studies are time-consuming and are therefore necessarily limited to a select number of compositions. Computational modeling has the potential to be quickly applied to many alloy systems, but the results should always be verified by experimental data. It is by marrying these 2 approaches that they can inform, and accelerate, one another. That is, computational results can be tuned by experimentally-derived parameters and experimental decisions can be informed by predicted results.

Nanocrystalline alloys present an important subset of metallic materials.[1] Because of their small grain size (less than 100 nm), they tend to possess extremely high strengths,[2–8] which are associated with grain boundary (GB) strengthening, i.e., the Hall–Petch effect.[9,10] Hence, these alloys can possibly enable new lightweight components, high-strength conductors, and many other applications that are not achievable using conventional coarse-grained alloys. A fundamental limitation to their use comes from their inherent thermal instability, which has been extensively explored using both experiments[11–19] and computational approaches.[20–32] The small grain size produces an extremely large driving force for grain growth. If not kept in check, grain growth can occur at modest temperatures, even at room temperature in pure materials, such as in copper and palladium.[33] Because nanocrystalline alloys are often produced via mechanical alloying,[34,35] this grain growth phenomenon provides a significant obstacle to consolidating the nanocrystalline powders by traditional powder metallurgy techniques where high-temperature sintering is common.

There are several methods that have been devised to circumvent this temperature sensitivity and to stabilize the grain size. Grain size stabilization commonly involves adding small quantities of an insoluble element (i.e., solute). Nonequilibrium processing (e.g., mechanical alloying, rapid solidification) is often used to force the solute into solution and, upon heating, the solute segregates to interfaces, such as GBs.[36,37] Alternatively, the solute remains in solution or precipitates out as a second phase. These 2 basic mechanisms for stabilization are known as thermodynamic stabilization and kinetic stabilization, respectively.[38] Thermodynamically, the solute is expected to segregate to GBs and reduce the GB energy to minimize or eliminate the driving force for growth.[39] Kinetically, the solute acts to hinder GB mobility by diffusion-related means, such as solute drag,[40] or by pinning boundaries with a fine dispersion of precipitates.[41]

The operating mechanism of stabilization can be difficult to delineate. Highly insoluble elements can segregate into interfaces, demix into discrete particles, or form intermetallic compounds with the solvent. The outcome depends on many different factors, such as elastic size mismatch between the solvent and solute and their enthalpy of mixing. To achieve thermodynamic stabilization, solute precipitation must be kinetically hindered.[39] Predicting and accounting for routes to grain size stabilization, then, is critical to deepening the understanding of grain size evolution in nanocrystalline alloys.

This work first focuses on the iron–zirconium (Fe–Zr) nanocrystalline alloys. In the nanocrystalline Fe–Zr system, experimental studies[14,16] have found that a nanoscale grain size in Fe could be maintained at 900 °C by adding 4 atomic percent (at%, or just % throughout this report) Zr. Without the Zr addition, the grain size in nanocrystalline Fe starts to coarsen near 400 °C. Zr was chosen as a solute because of its large atomic size difference with Fe (28%), which drives segregation. There is also a chemical contribution through the heat of mixing (-25 kJ mol^{-1}). This negative heat of mixing indicates that it is more favorable for Fe and Zr to form bonds between one another than to form bonds between like atoms. Hence, intermetallic formation is a likely outcome at high temperatures. Intermetallic formation is also a likely outcome in regions with high concentrations of Zr (e.g., interfaces). The competition between atomic segregation and second phase formation suggests that the Fe–Zr system must be considered from both thermodynamic and kinetic perspectives. In this manner, the Fe–Zr nanocrystalline system is similar to many nanocrystalline systems. As such, it is considered to be a representative nanocrystalline system for the present study.

The objective of the present work is to formulate a predictive thermokinetic model for grain growth. This objective is accomplished by extending the combined, thermokinetic model for grain growth[22,42,43] to allow for temperature dependence of parameters, thereby extending this model's predictive capability over a wide range of temperatures. The extended model is used to predict grain growth at a variety of temperatures and solute concentrations in the Fe–Zr system. The predictive modeling is then compared to X-ray diffraction data collected in situ during annealing of nanocrystalline Fe–Zr alloys with Zr (atomic) concentrations of 0.5%, 1%, 4%, and 10%. The present work shows the benefit of adding a temperature dependence to the thermokinetic model to predict grain growth for this system.

---

2. Thermokinetic Model for Grain Growth

The parabolic kinetics of grain growth are related to the presence of solute segregation to GBs and the drag force that results. In this scenario, the GB velocity, $V(= dD/dt)$, is controlled by the motion of single atoms through

$$V = \frac{dD}{dt} = v\lambda_{GBS}\text{exp}\left(-\frac{Q_d}{RT}\right)\left(1 - \text{exp}\left(-\frac{\Delta P}{RT}\right)\right), \tag{1}$$

where v is the jump frequency, λ_{GBS} is the spacing of atoms in the GB, R is the gas constant, T is the temperature, and Q_d is the activation energy for an atom to transfer from 1 grain to another under a driving force ΔP. We can assume that $\Delta P << RT$ for most cases and that $\Delta P \approx \gamma_b/D$ for curvature-induced grain growth processes, where γ_b is related to the GB energy. Additionally, the pre-exponential factor $v\lambda_{GBS}/RT$ is related to the interface mobility M_0, leading to the expression

$$\frac{dD}{dt} = M_0\frac{\gamma_b}{D}\text{exp}\left(-\frac{Q_d}{RT}\right). \tag{2}$$

To calculate M_0, Vooijs et al.[44] showed that $M_0 = v\lambda_{GBS}/RT = k\delta/hR$ with δ =3.0 Å, and h and k being the Planck's and Boltzmann's constants, respectively. This gives a mobility of 0.7518 $\text{mol m J}^{-1}\text{ s}^{-1}$ that is only dependent on the length scale parameter relating to interface width, δ. In Eq. 2, both Q_d and γ_b are functions of the temperature T and the solute concentration x_0, giving

$$\frac{dD}{dt} = M_0\frac{\gamma_b\left(T, x_0\right)}{D}\text{exp}\left(-\frac{Q_d\left(T, x_0\right)}{RT}\right). \tag{3}$$

It can be shown that Q_d and γ_b are interrelated. For instance, as solute segregates to the boundary, γ_b decreases, and there is an associated increase in Q_d because of solute drag effect. However, it is also important to realize that there are limits on Q_d and γ_b related to reaching a metastable equilibrium when a certain grain size D^* is reached (when $\gamma_b = 0$).

2.1 Thermodynamics of Grain Growth

The thermodynamics of grain growth is based on the concept that nanocrystalline materials can be stabilized against grain growth by GB segregation. This concept is related to the Gibbs adsorption equation and can be formally written as

$$\gamma_b = \gamma_0 - \Gamma_{b0}\left[RT\text{ln}\left(x_0 - \frac{3\Gamma_{b0}V_m}{D}\right) + \Delta H_{seg}\right], \tag{4}$$

where γ_0 is the GB energy for the case of a pure material, V_m is the molar volume of the alloy, ΔH_{seg} is the heat of segregation, Γ_{b0} is the saturated solute excess, and Γ_b is the solute excess at the boundary. Note that Γ_b is less than Γ_{b0} for the case where the GB is not saturated by solute and that these values are equal for the GB saturated case. The term γ_b is composed of 2 terms: the first reflects the GB energy in the absence of solute (γ_0); and the second larger term modifies γ_b by accounting for the energy reduction caused by segregation of solute.

Chen et al.[22,42] have applied a first order Taylor expansion of Eq. 4 and an equation of mass conservation for nanocrystalline materials ($\Gamma_{b0} = x_0\rho(D/6 + \delta)$) to obtain an expression for γ_0 in the unsaturated ($\Gamma_b/\Gamma_{b0} < 1$) and saturated cases ($\Gamma_b/\Gamma_{b0} = 1$) that is a function of the grain size D, i.e.,

$$\gamma_b = \gamma_1 + \gamma_2 \frac{1}{D}, \tag{5}$$

where

$$\gamma_1 = \begin{cases} \gamma_0 - \Gamma_{b0}\left[RT\left(\ln x_0 - \frac{V_m\rho}{2}\right) + \Delta H_{seg}\right], & \Gamma_b/\Gamma_{b0} < 1 \\ \gamma_0 - \Gamma_{b0}\left[RT\ln x_0 + \Delta H_{seg}\right], & \Gamma_b/\Gamma_{b0} = 1 \end{cases} \tag{6}$$

and

$$\gamma_2 = \begin{cases} 3\Gamma_{b0} RT V_m \rho\delta, & \Gamma_b/\Gamma_{b0} < 1 \\ 3\Gamma_{b0}^2 RT V_m/x_0, & \Gamma_b/\Gamma_{b0} = 1 \end{cases}. \tag{7}$$

The limiting case in the Chen et al. thermokinetic model [22,42] is that γ_0 must be equal to or greater than zero.

2.2 Kinetics of Grain Growth

The kinetic aspect of grain growth is based on the concept that grain growth occurs as a result of GB diffusion. Diffusion at the boundary is affected by solute interactions with the GB structure. Borisov et al.[45] derived the following expression for GB energy, i.e.,

$$\gamma_b = \left(\frac{kT}{\alpha a_0^2}\right) m_a \left[\ln\left(\frac{\delta\frac{D_D}{D_L}}{a_0\lambda^\alpha}\right) - \ln m_a\right], \tag{8}$$

where $\lambda = 1$, $\alpha(= 1)$ is for the interstitial mechanism, a_0 is the average interatomic distance, δ is the GB width, and m_a is the number of atomic layers forming the GB. The GB and lattice diffusion terms are D_D and D_L, respectively, and these can be given as

$$D_D = D_D^0 \exp\left(-\frac{Q_D}{RT}\right) \tag{9}$$

and

$$D_L = D_L^0 \exp\left(-\frac{Q_D}{RT}\right), \tag{10}$$

where D_D^0 and D_L^0 are the pre-exponential diffusion terms for D_D and D_L. Chen et al.[22,42] assume a monolayer coverage of the GB ($m_a = 1$), $\Gamma_{b0} = 1/\alpha a_0^2 N_a$, and $D_D^0 = D_L^0$ to rewrite γ_b as a function of Q_D, i.e., $\gamma_b = \Gamma_{b0}(Q_L - Q_D)$. Hence, the driving force for grain growth decreases with the increase of Q_D. The limiting case is when $Q_L = Q_D$, which results in $\gamma_b = 0$. In a similar form as γ_b, Q_D can be expressed as a function of grain size D, i.e.,

$$Q_D = Q_1 - Q_2\frac{1}{D}, \tag{11}$$

where

$$Q_1 = \begin{cases} Q_L + RT\ln\left(\frac{D_D^0}{D_L^0}\right) - \frac{\gamma_0}{\Gamma_{b0}} + \left(RT\left(\ln x_0 - \frac{V_m\rho}{2}\right) + \Delta H_{seg}\right), & \Gamma_b/\Gamma_{b0} < 1 \\ Q_L + RT\ln\left(\frac{D_D^0}{D_L^0}\right) - \frac{\gamma_0}{\Gamma_{b0}} + \left(RT\ln x_0 + \Delta H_{seg}\right), & \Gamma_b/\Gamma_{b0} = 1 \end{cases} \tag{12}$$

and

$$Q_2 = \begin{cases} 3RTV_m\rho\delta, & \Gamma_b/\Gamma_{b0} < 1 \\ 3\Gamma_{b0}RTV_m/x_0, & \Gamma_b/\Gamma_{b0} = 1 \end{cases}. \tag{13}$$

2.3 Thermokinetic Model

Chen et al.[22,42] show that by substituting Eqs. 5–7 and Eqs. 11–13 into Eq. 3, assuming that $\exp(-Q_2/RTD) \approx 1 + \sum_{i=1}^{n} 1/i!(-Q_2/RTD)^i$, and using boundary conditions of $t = 0$, $D = D_0$, $t = t$, and $D = D(t)$, they arrive at an expression for the evolution of grain size with time, i.e.,

$$\begin{gathered} \tfrac{1}{2}\left[\left(D + \tfrac{\gamma_2}{\gamma_1}\right)^2 - \left(D_0 + \tfrac{\gamma_2}{\gamma_1}\right)^2\right] - \left(\tfrac{Q_2}{RT} + \tfrac{2\gamma_2}{\gamma_1}\right)(D - D_0) + \left[\tfrac{\gamma_2^2}{\gamma_1^2} + \tfrac{\gamma_2}{\gamma_1}\tfrac{Q_2}{RT} + \tfrac{1}{2}\left(\tfrac{Q_2}{RT}\right)^2\right]\ln\left(\tfrac{\gamma_1 D + \gamma_2}{\gamma_1 D_0 + \gamma_2}\right) \\ = \gamma_1 M_0 \exp\left(-\tfrac{Q_1}{RT}\right)t, \end{gathered} \tag{14}$$

which can be reduced to

$$\begin{gathered} \tfrac{1}{2}\left(D^2 - D_0^2\right) - \tfrac{Q_2}{RT}(D - D_0) + \left[\tfrac{\gamma_2^2}{\gamma_1^2} + \tfrac{\gamma_2}{\gamma_1}\tfrac{Q_2}{RT} + \tfrac{1}{2}\left(\tfrac{Q_2}{RT}\right)^2\right]\ln\left(\tfrac{\gamma_1 D + \gamma_2}{\gamma_1 D_0 + \gamma_2}\right) \\ = \gamma_1 M_0 \exp\left(-\tfrac{Q_1}{RT}\right)t \end{gathered}. \tag{15}$$

Interestingly, the $D^2 - D_0^2$ term is of a similar form to the simple power law ($D^2 - D_0^2 = 2M_0\gamma_b t$) of Burke and Turnbull,[46] but the rest of the equations terms stem from the interaction between the kinetic and thermodynamic aspects of grain growth.

Table 1 Thermokinetic model variables and values

Variable	Value	Units
R	8.3145	$\mathrm{J\,mol^{-1}\,K^{-1}}$
h	$6.626\,068 \times 10^{-31}$	$\mathrm{m^2\,g\,s^{-1}}$
k	$1.380\,650\,3 \times 10^{-20}$	$\mathrm{m^2\,g\,s^{-2}\,K}$
N_A	$6.022\,141\,29 \times 10^{23}$	$\mathrm{mol^{-1}}$
λ	1	
α	1	
m_a	1	
a_0	8×10^{-10}	m
$\delta\,(= m_a a_0)$	8×10^{-10}	m
λ_{GBS}	3×10^{-10}	m
D_0	5×10^{-9}	m
D_D^0/D_L^0	1	
M_0	0.7518	$\mathrm{mol\,m\,J^{-1}\,s^{-1}}$

2.4 Model Implementation

The present model was applied to the Fe–Zr system. Tables 1 and 2 list the constants and values that were used in our initial calculations of the Fe–Zr system to validate the model with experimental Fe–Zr results. Table 1 lists most of the constants for the model. Notice that many of the parameters are not sensitive to the type of material system; several assumptions are made. First, m_a assumes a monolayer of solute at the GB; this may be different in some cases. Second, the initial grain size D_0 is 5 nm. Third, the mobility term M_0 is a material-independent parameter in the present model.

Table 2 Thermokinetic model material parameters constants and values

Variable	Value	Units
V_m	7.1×10^{-6}	$\mathrm{m^3\,mol^{-1}}$
ρ_{Fe}	7.87×10^{6}	$\mathrm{g\,m^{-3}}$ (original units)
Z_{Fe}	55.847	$\mathrm{g\,mol^{-1}}$ (original units)
$\rho = \rho_{Fe}/Z_{Fe}$	1.4092×10^{5}	$\mathrm{mol\,m^{-3}}$ (correct units)
T	1073	K
x_0	0.04	
γ_0	0.73	$\mathrm{J\,m^{-2}}$
ΔH_{seg}	$92\,400$	$\mathrm{J\,mol^{-1}}$
Q_L	$334\,800$	$\mathrm{J\,m^{-1}}$
Γ_{b0}	1.25×10^{-5}	$\mathrm{mol\,m^{-2}}$

Table 2 lists most of the material parameters constants for the model. The upper part of Table 2 lists a few easily obtained material constants: the molar volume V_m and the material density ρ_{Fe}. These constants are assumed to be equal to pure Fe, which may not be valid for high concentrations of solute. The lower part of Table 2 lists the state variables (temperature T and concentration x_0) as well as some of the thermokinetic parameters: GB energy of pure Fe γ_0, heat of segregation ΔH_{seg}, activation energy in the lattice Q_L, and the GB saturated solute excess Γ_{b0}.

The model was implemented with the following constants by setting Eq. 14 equal to zero, i.e.,

$$\begin{array}{c} f(D) = \frac{1}{2}\left[\left(D+\frac{\gamma_2}{\gamma_1}\right)^2 - \left(D_0+\frac{\gamma_2}{\gamma_1}\right)^2\right] - \left(\frac{Q_2}{RT}+\frac{2\gamma_2}{\gamma_1}\right)(D-D_0) \\ + \left[\frac{\gamma_2^2}{\gamma_1^2}+\frac{\gamma_2}{\gamma_1}\frac{Q_2}{RT}+\frac{1}{2}\left(\frac{Q_2}{RT}\right)^2\right]\ln\left(\frac{\gamma_1 D+\gamma_2}{\gamma_1 D_0+\gamma_2}\right) - \gamma_1 M_0 \exp\left(-\frac{Q_1}{RT}\right)t = 0 \end{array} . \tag{16}$$

A numerical method for root finding can now be used to solve for grain size D as a function of time t in this equation. The bisection root finding technique was employed herein. A brief description of the numerical method follows. The pseudocode for the bisection root finding technique is given in Fig. 1, where the function f is equal to Eq. 16, xLower is D_0, and xUpper is D^* $(= -\gamma_2/\gamma_1)$, and the root is equal to the value of D where $f(D) = 0$. The bisection method is an iterative technique that assumes the root to an equation f is located within a certain interval bounded by xLower and xUpper. Hence, f (xLower) and f (xUpper) have opposite signs. If an intermediate coordinate is chosen (xMid), the sign of f (xMid) narrows down the interval where the root exists (i.e., if f (xLower) and f (xMid) have opposite signs, the root lies in the interval $[\text{xLower}, \text{xMid}]$, and if they have the same signs, then the root lies in $[\text{xMid}, \text{xUpper}]$). This process continues to subdivide the interval where the root is until it has been reduced to a specified tolerance, xTol. While other root finding methods may be more efficient (e.g., False Position, Newton–Rhapson, Secant), the present thermokinetic model is not expensive and the bisection method converges to the root within a specified tolerance.

```
Input xLower, xUpper, xTol
yLower = f(xLower)
xMid = (xLower + xUpper)/2.0
yMid = f(xMid)
iters = 0
While ( (xUpper - xLower)/2.0 < xTol )
    iters = iters + 1
    if( yLower * yMid > 0.0) Then xLower = xMid
    Else xUpper = xMid
    Endofif
    xMid = (xLower + xUpper)/2.0
    yMid = f(xMid)
Endofwhile
Return xMid, yMid, iters (* xMid = approximation to root *)
```

Fig. 1 Pseudocode for bisection root finding algorithm

To validate that the present thermokinetic model agrees with that of Chen et al.,[22,42] the thermokinetic model was plotted using the parameters from Tables 1 and 2 along with the experimental data from Darling et al.[16] in Fig. 2. The saturated formulation of the thermokinetic model was used, although the unsaturated model yields the same curve with slightly different values of ΔH_{seg} ($+3.5\%$) and Q_L (-3.0%). The thermokinetic model agrees well with the experimental data and the model implementation agrees with that of Chen et al.[22,42] Moreover, this model for nanocrystalline grain growth assumes both kinetic and thermal contributions, in agreement with experimental findings of Darling et al.[16] In the remainder of this report, we examine the sensitivity of the thermokinetic model to input parameters and discuss extending it towards predicting nanocrystalline grain growth at a variety of temperatures and solute concentrations.

Optimization in the present analysis uses an unconstrained nonlinear optimization algorithm,

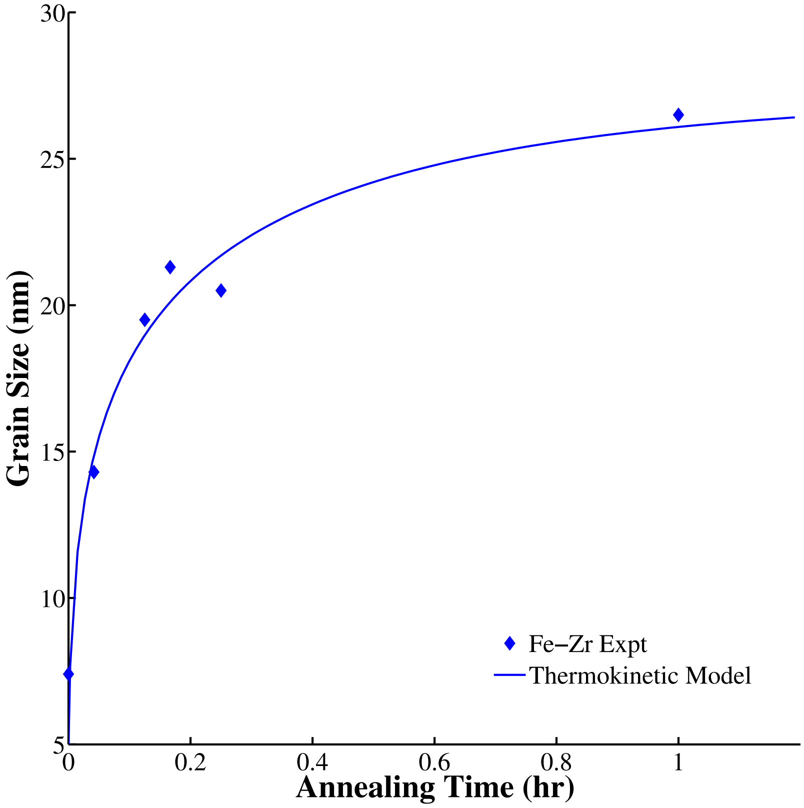

Fig. 2 Evolution of the average grain size as a function of annealing time for nanocrystalline Fe–4% Zr alloy annealed at 800 °C (1,073 K)

i.e., the Nelder-Mead simplex algorithm.[47] This algorithm uses a simplex of $n + 1$ points for n-dimensional vectors x. The algorithm first makes a simplex around the initial guess x_0 by adding 5% of each component $x_0(i)$ to x_0, and using these n vectors as elements of the simplex in addition to x_0. Then, the algorithm modifies the simplex repeatedly until it meets a stopping criterion and obtains a solution x_{sol}. Some of the basic MATLAB codes for the thermokinetic model and its optimization with the temperature dependence are attached in Appendices A–C.

3. Experimental Fe–Zr Results

3.1 X-ray Diffraction (XRD) Measurements of Grain Growth in Nanocrystalline Fe

This section discusses a newly-acquired XRD dataset for Fe–Zr alloys with various concentrations of Zr (0.5% Zr, 1% Zr, 4% Zr, 10% Zr) and at various annealing temperatures (700, 800, 900, and 1,000 °C). Currently, the thermokinetic model for Fe–Zr has only been applied to a nanocrystalline Fe–4% Zr alloy at 800 °C. To illustrate the difficulty of high-temperature processing of nanocrystalline materials in pure α-Fe and to establish a baseline for grain growth, a nanocrystalline-Fe sample with a nominal grain size of 5 nm was annealed at temperatures of 400, 500, 600, and 700 °C (Fig. 3). The lines are included as a guide to the eye for the XRD data at different annealing temperatures. At temperatures of greater than 400 °C, there is appreciable grain growth in the nanocrystalline Fe material; at temperatures of 600 and 700 °C, there is more than an order of magnitude of difference in grain size after annealing for 1 h (3600 s). These results are in good agreement with prior work on nanocrystalline Fe, which has exhibited grain growth at temperatures around 500 °C. In the following section, we discuss the process used for the nanocrystalline structures, the microstructure and operating mechanisms for grain growth, and the data obtained for various concentrations of Zr in the Fe–Zr alloys.

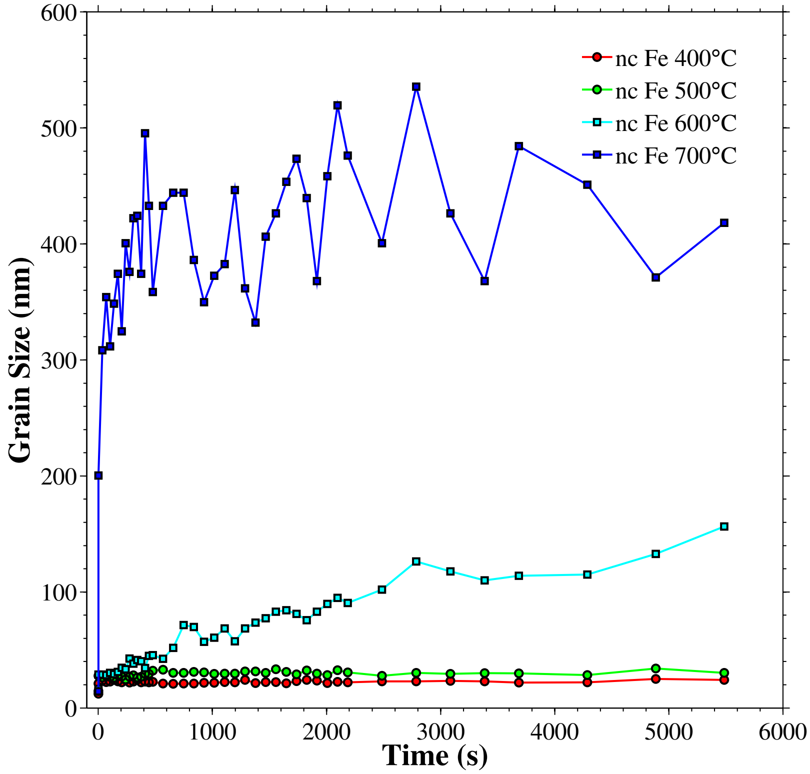

Fig. 3 Evolution of the average grain size as a function of annealing time at multiple temperatures (400–700 °C) for unalloyed nanocrystalline Fe

3.2 Grain Growth in Nanocrystalline Fe

The processing and microstructure of these samples helps explain the observed X-ray behavior. During high-energy mechanical alloying, nanoscale microstructures are generated by the accumulation of severe, localized plastic deformation. After reaching a certain level of strain, dislocation cell structures and small angle GBs approximately 25 nm in size form. Continued mechanical attrition forms smaller grains within the entire volume of the material.[48,49] This initial grain size distribution changes upon grain growth at high temperatures; the magnitude and direction of the grain size distribution is dependent on the evolved representative population. The change in population can occur in 2 primary ways: normal and abnormal grain growth.[50]

An ideal grain structure exhibits normal microstructure growth that occurs continuously and uniformly; this structure is also held in this state by a radius-dependent counterbalancing effect. However, grains with diameters much larger or smaller than the normal size distribution grow at rates that eventually cause them to rejoin the collective population.[50] In this basic model of grain growth, the GB area reduction and the corresponding energy reduction drives the growth rate. In nanocrystalline materials, size-dependent microstructure features, such as triple lines and quadruple points, can kinetically hinder self-similar grain growth as well.[51] Abnormal grain growth, however, proceeds in a much different manner. Here, the controlling mechanisms allow select grains some growth advantage over neighboring grains; consequently, accelerated growth of these select grains occurs at the cost of consuming the much smaller surrounding grains.[50]

Abnormal grain growth plays a significant role in controlling the stability and growth kinetics of nanocrystalline microstructures. In this work, the grain growth observed in nanocrystalline Fe (Fig. 3) can be controlled through adding a solute element (e.g., Zr) that segregates to the GBs. Hence, in the Fe–Zr system reported here, grain growth is controlled by solute-influenced mechanisms, such as second phase particle pinning and/or inhomogeneous solute drag effects. Inhomogeneous solute drag effects can arise from a high dependency of GB composition on its inherent structure and orientation.[52] In a sample composed of a large distribution of GB configurations, local regions of anisotropy in GB composition exist. GBs represent a finite volume (e.g., based on GB area and width) within the material for segregating elements to occupy. At small grains sizes (more volume) and low solute concentrations (less segregant), the distribution of the segregating species to the boundaries is expected to be less uniform, which leads to more abnormal grain growth.

At elevated temperatures, nanocrystalline Fe and Fe–Zr alloys undergo bimodal grain growth where both larger, abnormal grains and nanoscale grains coexist.[16,53] While transmission electron microscopy can supply detailed information about grain size over a relatively small area, the X-ray diffraction technique used in the present study can supply in situ information about the volume-averaged grain size and grain growth over much larger areas, encompassing both of the aforementioned modes of grain growth. X-ray line broadening analysis takes advantage of the fact that, below approximately 100 nm, small crystallites cause broadening or an angular divergence of the diffracted beam at angles near the specific Bragg angle.[54] Therefore, in a given sample volume, regions containing crystallites much larger 100 nm do not contribute to the overall broadening observed. Thus, line broadening analysis for grain size estimates is sensitive only to the volume fraction of the microstructure containing nanocrystalline grains. Although, it should be noted that the accuracy of the X-ray diffraction technique may decrease for average grain sizes larger than 50 nm as abnormal grain growth and second phase formation may occur.

Further supporting the XRD measurements in Fig. 3, recent results have shown that nanocrystalline Fe, prepared by mechanical milling and annealed isothermally in a tube furnace under forming gas, undergoes extensive growth abnormally at 600 °C.[53] The resultant microstructure was found to consist of regions containing 50% ultrafine (100–300 nm) grains and

50% coarse, micron grains (approximately 6 μm). By 700 °C, nanocrystalline Fe was shown to be entirely transformed to a microstructure containing micron-sized grains.[53] Figure 3 reveals that in situ heating during X-ray analysis has similar results to that reported earlier.

The microstructure evolution for pure, nanocrystalline Fe, after annealing at 600 and 700 °C during high-temperature X-ray experiments, clearly displays both normal and abnormal grain growth (Fig. 4). These images are etched to reveal regions of abnormal grain growth, which are the white or gray regions with smooth contrast (indicated by white arrows), while the nanometer or ultrafine grained regions are the gray regions with a rough or granulated contrast (indicated by black arrows).[16,53] Figure 4a, taken after annealing pure nanocrystalline Fe at 600 °C, shows that the microstructure has undergone extensive grain growth. At 600 °C, abnormally grown grains (average size of 15 μm) represent a significant fraction of the microstructure while the remaining fraction is nanocrystalline or ultrafine grained. Annealing at 700 °C (Fig. 4b) caused the entire microstructure to undergo abnormal grain growth, resulting in an average grain size much larger than at 600 °C.

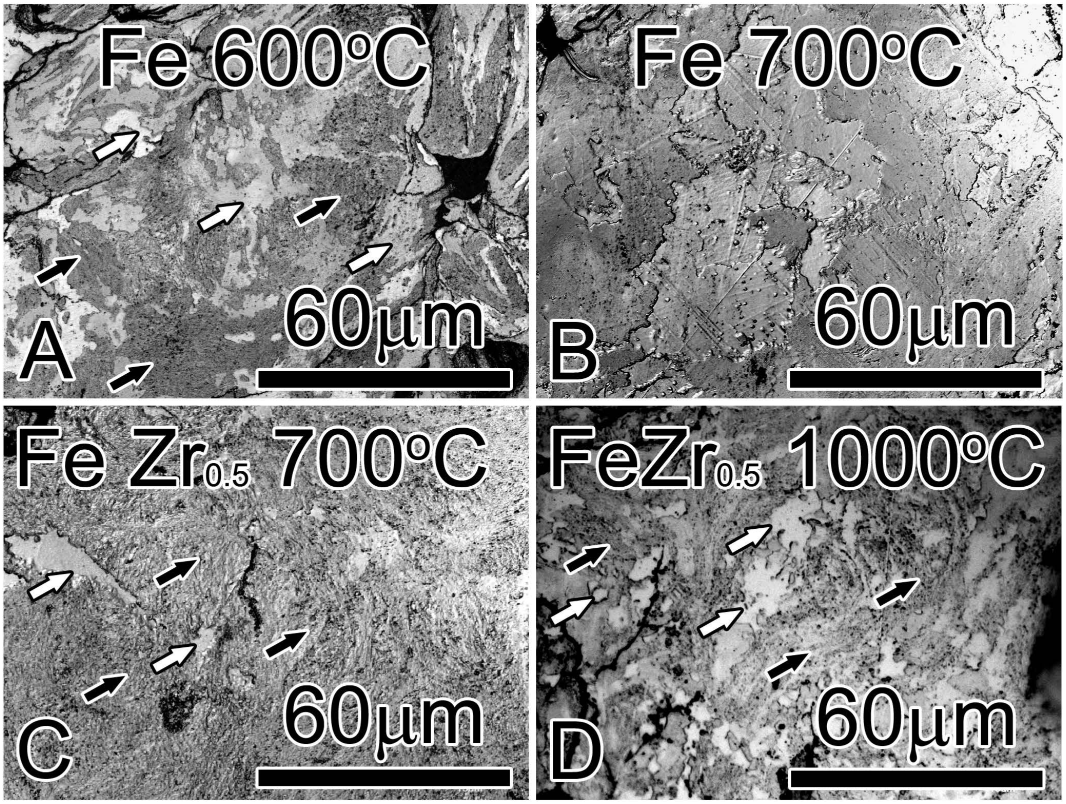

Fig. 4 Evolution of the microstructure as a function of annealing time at multiple temperatures (600, 700, and 1,000 °C) for nanocrystalline Fe and Fe–0.5% Zr alloy

3.3 XRD Measurements of Grain Growth in Nanocrystalline Fe–Zr

The XRD datasets for nanocrystalline Fe–Zr alloys at higher temperatures than for nanocrystalline Fe were also obtained. The volume-averaged grain size data as a function of annealing time are shown in Fig. 5 for the various Fe–Zr alloys and temperatures. It is important to point out a few differences between Fig. 3 and Fig. 5. First, the scale bar for the grain size is exactly 1 order of magnitude lower in Fig. 5 (i.e., the maximum grain size for the y-axis was reduced from 600 nm to 60 nm). Second, the annealing temperatures are much higher in Fig. 5 (i.e., the range of temperatures was increased from 400–700 °C to 700–1,000 °C). Interestingly, the smallest (0.5% Zr) and largest (10% Zr) concentrations of Zr have the smallest stabilized grain sizes for 700–900 °C range. However, in both of these Fe–Zr systems, there is very different behavior at 1,000 °C, which may be attributed to second phase formation (10% Zr) or sufficient kinetic energy to overcome the influence of Zr on stabilizing the GBs (0.5% Zr). The present dataset is used for fitting the thermokinetic model.

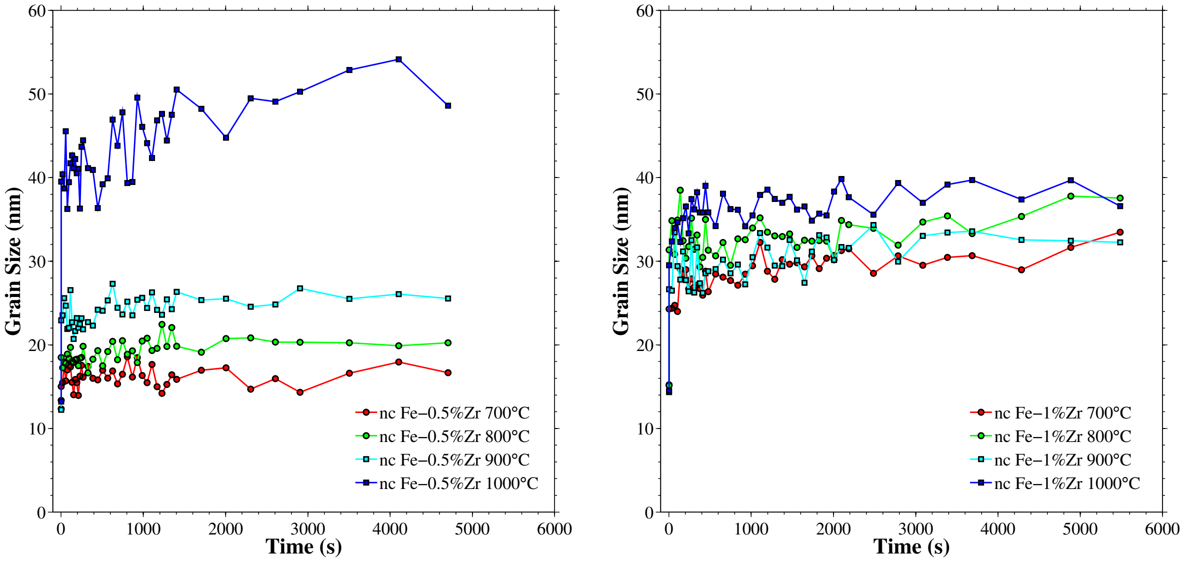

(a) Fe–0.5% Zr **(b)** Fe–1% Zr

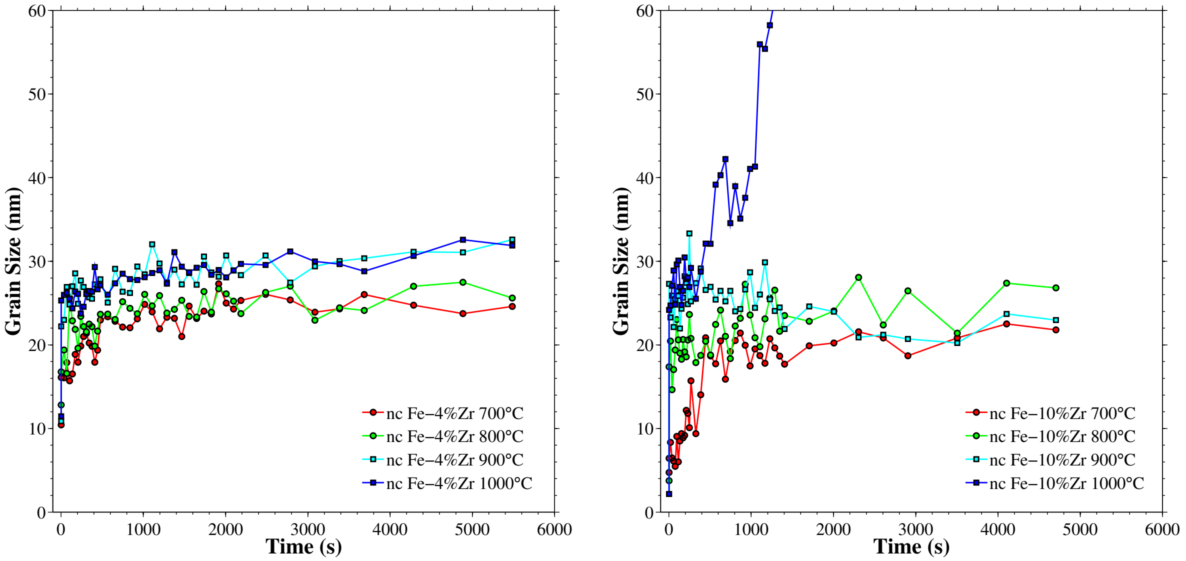

(c) Fe–4% Zr **(d)** Fe–10% Zr

Fig. 5 Evolution of the average grain size as a function of annealing time at multiple temperatures (700–1,000 °C) for nanocrystalline Fe–Zr alloy with different Zr concentrations: a) 0.5% Zr, b) 1% Zr, c) 4% Zr, d) 10% Zr

3.4 Grain Growth in Nanocrystalline Fe–Zr

The addition of Zr as a solute in Fe has been shown to stabilize the grain size to high homologous temperatures.[14,16,53] The stability was observed to increase with Zr content, up to 10 at% Zr where the precipitation of equilibrium intermetallics was exceedingly favorable.[14] The increase in stability with solute content followed by precipitation of intermetallics and loss of stability have been used to delineate a system and its extent of being thermodynamically stable by many authors.[38] It is thus expected that the concentration of stabilizing solute plays a critical role in the overall evolution of such microstructures at elevated temperatures. Darling et al. have reported that an increase in Zr content leads to a smaller retained grain size within the nanoscale regions of the microstructure and to some extent controls the level of abnormal grain growth.[16] Additionally, the concentration of the Zr solute has been observed to influence the grain morphology. Low Zr contents (1/3 at%) led to acicular-type grains with aspect ratios greater than 5 in some cases, while higher Zr concentrations (1–4 at%) led to more equiaxed structures. The amount of solute also directly impacts the as-milled grain size.[55,56]

In addition to compositional effects, it has also been proposed that the body-centered cubic (bcc) to face-centered cubic (fcc) phase transition may be another point of system instability.[57,58] Figure 4 is in line with these results. Figure 4c shows the etched micrographs of Fe–0.5 at% Zr after annealing at 700 °C and 1,000 °C, in which there are only a few small regions that have evidence of abnormal grain growth. The fraction of the microstructure abnormally grown after annealing at 700 °C, as estimated from lower magnification micrographs, was found to be less than 3%. This is a stark improvement over pure Fe. However, after annealing at 1,000 °C, the Fe–0.5 at% Zr alloy (Fig. 4d) has undergone extensive abnormal grain growth. Samples containing greater than 0.5 at% Zr show limited abnormal growth (less than 5% of the area), even at temperatures as high as 1,000 °C. It is expected that the 10 at% Zr sample is heavily precipitated. In this case, kinetic pinning by a secondary phase dominates the microstructural stability; such a mechanism is not captured by the current model.

Since lower Zr solute contents (0.5 at%) result in bimodal microstructures having large areas of abnormal growth and regions where the morphology of the nanoscale grains may be largely distorted, the reported model is not expected to fit this data well. Additionally, the 10 at% Zr data are most likely heavily precipitated, giving rise to Zener pinning; such growth kinetics are also not captured within the current model. Hence, the XRD data from 1 at% and 4 at% Zr—where the majority of the grain growth is expected to be normal, that is, controlled by both thermodynamics and kinetics (solute drag)—are ideal experimental datasets for the present model. It is expected that the 1 at% and 4 at% Zr samples contain sufficient solute to evenly coat the GB, without being high enough to kinetically promote precipitation of secondary phases.[38]

4. Model Results

4.1 Parameter Sensitivity Analysis

The sensitivity analysis of a model is a local measure of the effect of a given input (or parameter) on a given output (in this case, the evolution of grain size with time). Another definition of sensitivity analysis is, “The study of how the uncertainty in the output of a model can be apportioned to difference sources of uncertainty in the model input”, i.e., it is important to know which parameters affect the output and the magnitude of this interaction. Prior to fitting to the XRD datasets described in Section 3, some of the material parameters, which were used within the thermokinetic model for Fe–4% Zr model at 800 °C, were perturbed to understand their influence on the grain size and the shape of the grain size-annealing time curve. There are several methods for examining parameter sensitivity since the sensitivity is typically defined as $S_j = \partial Y / \partial X_j$, where Y is the output and X_j is the jth parameter. From a local perspective, parameter X_j can be locally adjusted around some default value while all other parameters are held fixed to quantify the change in output Y. From a global perspective, though, it may be important to know the effect of parameter X_j on the output Y while all other parameters $X_{i \neq j}$ are also varying (e.g., a Monte Carlo approach or the Morris one-factor-at-a-time approach). It should be noted that instead of a scalar value for the output Y, in this study Y is a function of time; hence, the sensitivity of grain size to a particular parameter may change with time. The local and global sensitivity analyses are briefly explored in Sections 4.1.1 and 4.1.2. Additionally, the change in this behavior as a function of different temperatures and concentrations of Zr is also investigated in Section 4.1.3.

4.1.1 Local Sensitivity Analysis

The local sensitivity of the parameters was examined by selecting a baseline set of parameter values (the Fe–4% Zr model at 800 °C) and iteratively varying each by different percentages (e.g., -1%, +1%, +2%, +3%) to qualitatively observe their effect on the grain size evolution curves. The subsequent global sensitivity analysis in Section 4.1.2 will use a Monte Carlo analysis to quantify the sensitivity of grain size to each parameter (in combination with the other parameters varying) as a function of time.

The change in the grain growth behavior as a function of deviations from the material parameters utilized in the present Fe–4% Zr model at 800 °C (i.e., γ_0, ΔH_{seg}, Γ_{b0}, and Q_L) are shown in Fig. 6. In each subplot, the blue line represents the baseline and the green and red lines indicate deviations from these baseline values (Table 2) in increments of $+1\%$ and -1%, respectively. First, increasing γ_0 results in an increase in the equilibrium grain size D^* and a corresponding increase in grain growth behavior. However, for all other parameters, an increase corresponds to a decrease in both D^* and the grain growth behavior. The time scale associated with reaching the stabilized grain size correspondingly decreases/increases with D^*. Second, the rate of deviation from the baseline grain growth plot (in terms of deviation at large times) for a 1% deviation in material parameters (i.e., the sensitivity) follows this order: ΔH_{seg} (largest), γ_0, Γ_{b0}, and Q_L (smallest). However, while the activation energy Q_L has the smallest effect at larger times, it has a dramatic effect on the shape of the grain growth curve at shorter times (i.e., there is a greater sensitivity to Q_L at shorter times). In fact, for lower activation energies, the thermokinetic model starts to approach the behavior of the thermokinetic model without the GB energy effect, i.e., the Gong et al.model.[25] Notice that, in some cases, only a few red or green curves are generated. In each case, 10 increments of $\pm 1\%$ were attempted. However, there is a limit that these variables can be increased/decreased that corresponds to a regime where the stabilized grain size D^* $(= -\gamma_2/\gamma_1)$ becomes either lower than the initial grain size (i.e., $\gamma_2 < -D_0\gamma_1$, no grain growth) or negative (i.e., both γ_1 and γ_2 are positive, no stabilized grain size).

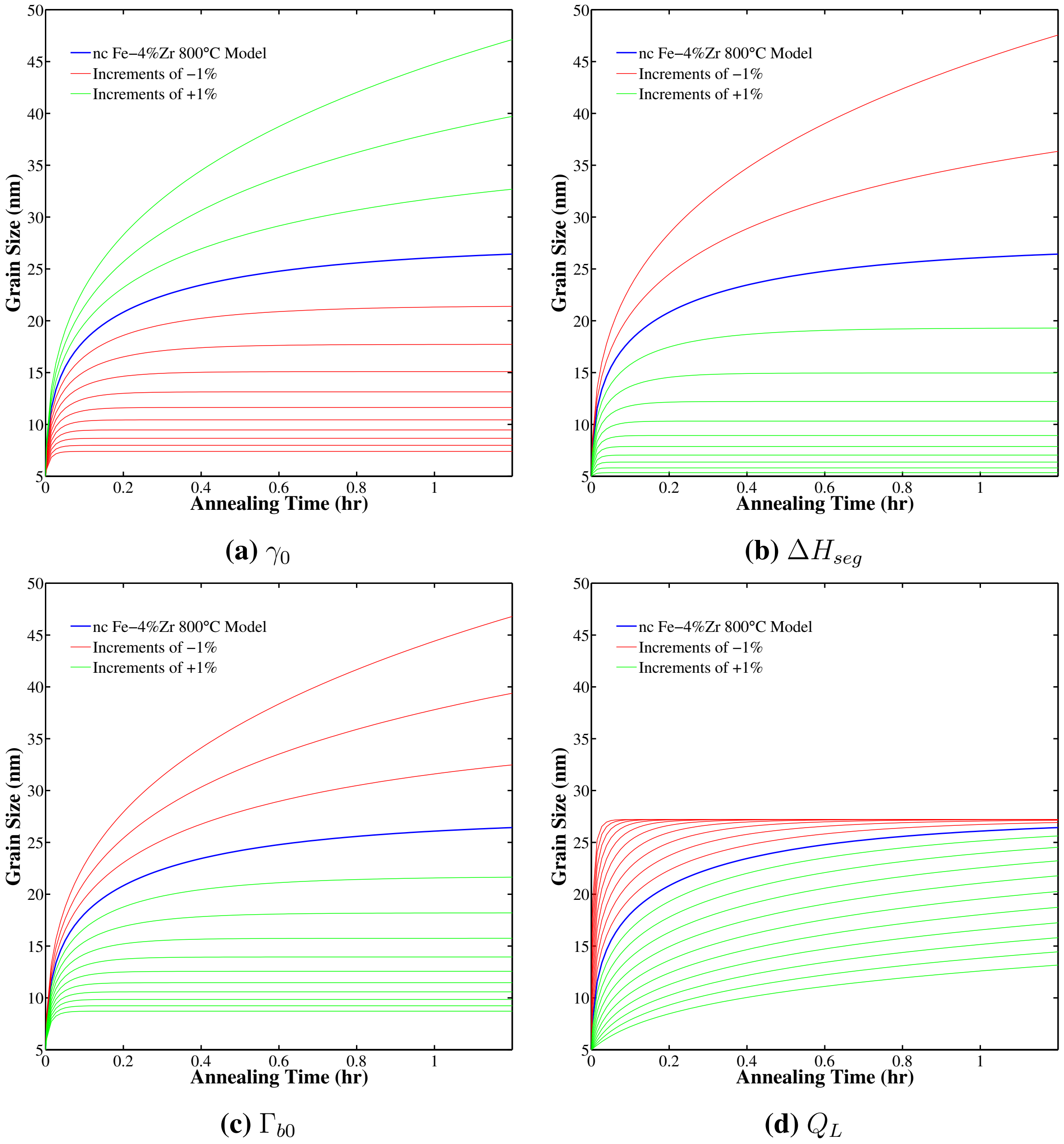

(a) γ_0 **(b)** ΔH_{seg}

(c) Γ_{b0} **(d)** Q_L

Fig. 6 Evolution of the average grain size as a function of annealing time for nanocrystalline Fe–4% Zr alloy annealed at 800 °C (1,073 K). The different plots (a–d) show the thermokinetic model with the parameters listed in Tables 1 and 2 and the new curves generated by changing the value of one of the parameters (in increments of $\pm 1\%$): a) γ_0, b) ΔH_{seg}, c) Γ_{b0}, and d) Q_L.

The rate of grain growth can also be calculated from the preceding analysis as a function of annealing time, as shown in Fig. 7. A central difference numerical method was used to calculate the derivative of the grain growth curves (Fig. 6). Similar trends are observed. Interestingly, the activation energy again shows a large influence on the rate of grain growth in the beginning stages of annealing. In fact, while ΔH_{seg}, γ_0, and Γ_{b0} show a scaling behavior in terms of the rate of grain growth, the Q_L plot shows very different behavior. For increasing Q_L, the rate of grain growth is decreased as with the other material parameters. However, for decreasing Q_L, there are 2 regimes: a regime of accelerated grain growth rates at short times, and a regime where grain growth is lower than the baseline. In this manner, the activation energy Q_L controls the kinetics for obtaining the stabilized grain size without actually modifying D^* (i.e., modifies the shape of the grain growth curve, as can be seen in Fig. 6).

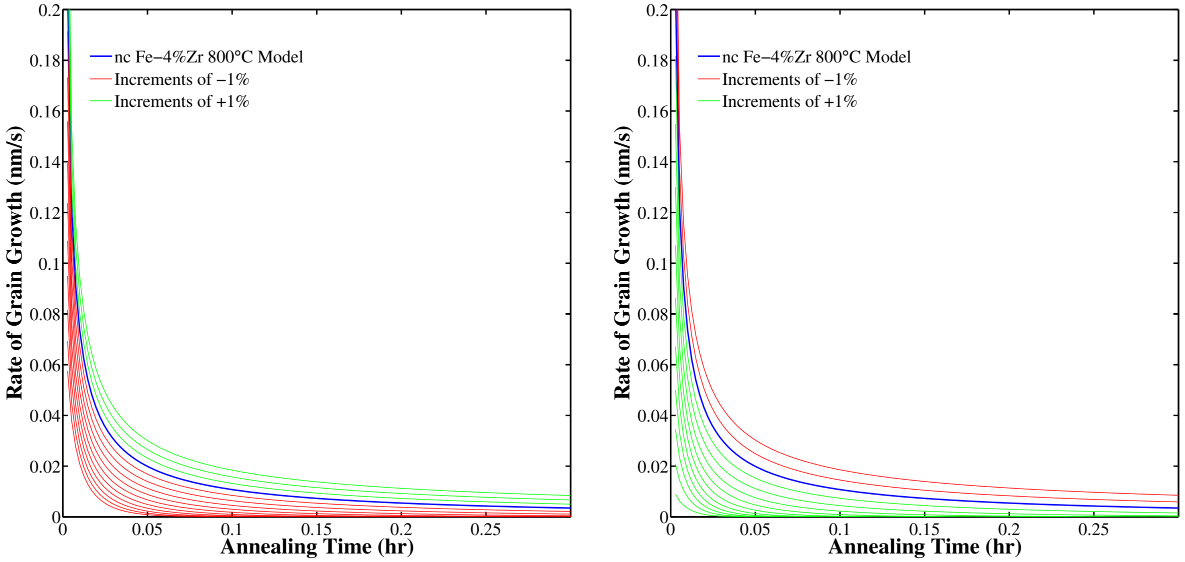

(a) γ_0 **(b)** ΔH_{seg}

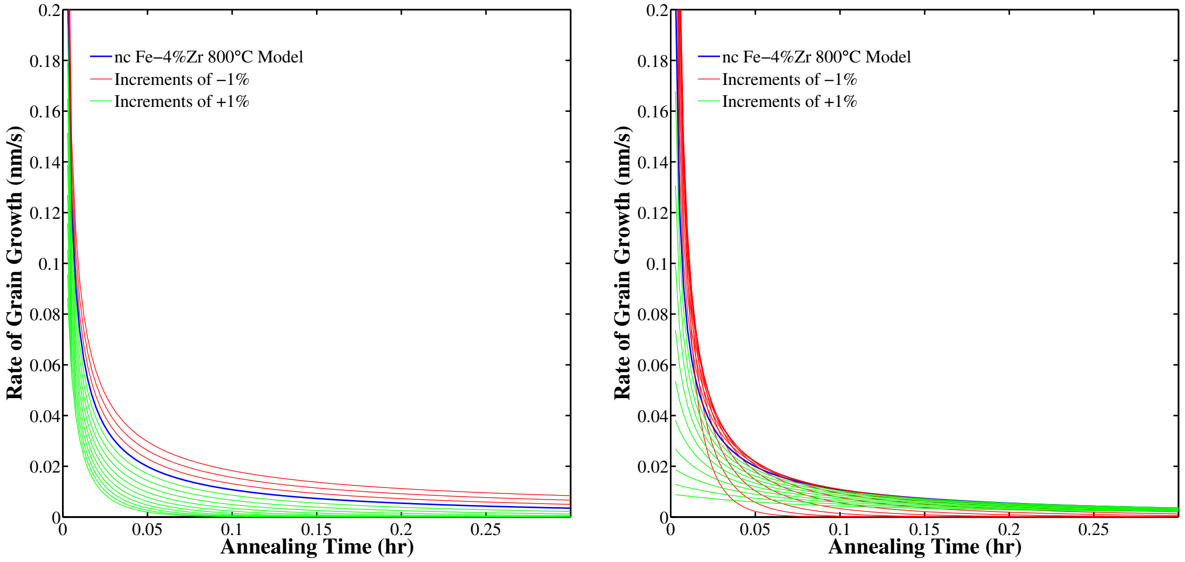

(c) Γ_{b0} **(d)** Q_L

Fig. 7 Evolution of the rate of grain growth as a function of annealing time for nanocrystalline Fe–4% Zr alloy annealed at 800 °C (1,073 K). In a similar manner to Fig. 6, the different plots (a–d) show the thermokinetic model with the parameters listed in Tables 1 and 2 and the new curves generated by changing the value of one of the parameters (in increments of $\pm 1\%$): a) γ_0, b) ΔH_{seg}, c) Γ_{b0}, and d) Q_L.

Additionally, the influence of additional parameters in the thermokinetic model can be explored. For instance, the effect of the mobility term, M_0, on the grain growth curves is shown in Fig. 8. In these plots, 10 increments of $\pm 10\%$ were used to explore the effect of the mobility term on grain growth. Hence, the upper bound for the green curves represents doubling the mobility term ($+100\%$) and the lower bound of the red curves represents a mobility of 0 (-100%), i.e., no grain growth. Interestingly, the mobility behaves very similar to the activation energy Q_L; high mobilities favor fast grain growth without changing the stabilized grain size. However, while the mobility results in changes similar to the activation energy, much larger increases in mobility are required to make a substantial change in the grain growth behavior (i.e., the thermokinetic model is relatively insensitive to M_0).

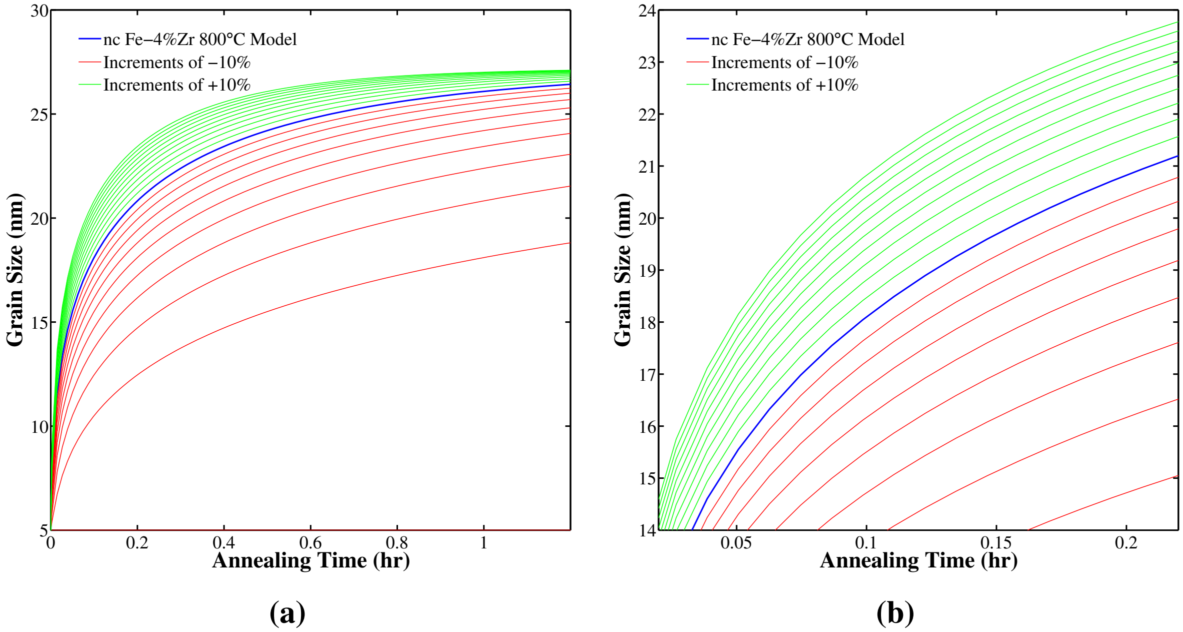

(a) **(b)**

Fig. 8 Evolution of the average grain size as a function of annealing time for nanocrystalline Fe–4% Zr alloy annealed at 800 °C (1,073 K). The different plots show the thermokinetic model with the parameters listed in Tables 1 and 2 and the new curves generated by changing the mobility term M_0 (in 10 increments of $\pm 10\%$).

The preceding analysis shows that a fit of the material parameters to experimental grain growth data does not result in a unique set of material parameters (e.g., γ_0, Γ_{b0}, ΔH_{seg}, Q_L). For instance, using the parameters outlined for the Fe–4% Zr at 800 °C, the GB energy term γ_0 was modified by multiplying it by 0.97 to 1.03 in increments of 0.01. The initial curve was used as a baseline curve and a curve with the new value of γ_0 was fit to the original curve using only the enthalpy change ΔH_{seg} and activation energy Q_L (Table 3). The new curves were virtually indistinguishable from the baseline grain growth curve. Interestingly, the activation energy Q_L was unchanged and only the enthalpy change ΔH_{seg} was modified. This result agrees with Fig. 6; i.e., the activation energy modifies the shape of the curve and γ_0, ΔH_{seg}, and Γ_{b0} all modify the magnitude of the grain size for the thermokinetic model. Moreover, there is a linear dependence between γ_0 and ΔH_{seg} for non-unique solutions, e.g., $\gamma_0 = c\Delta H_{seg}$ with $c = 8.175 \times 10^{-6}\ \mathrm{mol\,m^{-2}}$. The saturated excess Γ_{b0} was held constant in the present analysis, but Γ_{b0} is likely to have a similar effect to ΔH_{seg} based on Fig. 6.

Table 3 Non-unique material parameter set for Fe–4% Zr at 800 °C

Parameter	Symbol	$0.97\gamma_0$	$0.98\gamma_0$	$0.99\gamma_0$	γ_0	$1.01\gamma_0$	$1.02\gamma_0$	$1.03\gamma_0$
GB energy ($\mathrm{J\,m^{-2}}$)	γ_0	0.708	0.715	0.723	0.73	0.737	0.745	0.752
Saturated excess ($10^{-5}\ \mathrm{mol\,m^{-2}}$)	Γ_{b0}	1.25	1.25	1.25	1.25	1.25	1.25	1.25
Enthalpy change ($\mathrm{kJ\,mol^{-1}}$)	ΔH_{seg}	87.5	88.1	88.7	89.3	89.9	90.5	91.1
Activation energy ($\mathrm{kJ\,mol^{-1}}$)	Q_L	345.1	345.1	345.1	345.1	345.1	345.1	345.1

4.1.2 Global Sensitivity Analysis

The global sensitivity analysis of the parameters can be explored using a number of different methods. Herein, we have used a Monte Carlo approach that has been coupled with scatter plots, regression modeling, and correlation coefficients to show the sensitivity of the grain size evolution to the model parameters. For the present analysis, 6 parameters were varied within the Monte Carlo simulations: ΔH_{seg} (heat of segregation), Q_L (activation energy), γ_0 (initial grain boundary energy), Γ_{b0} (saturated solute excess), M_0 (grain boundary mobility), and D_0 (initial grain size). The last 2 parameters were included to show the relative sensitivity of the thermodynamic and kinetic parameters (ΔH_{seg}, Q_L, γ_0, Γ_{b0}) to the material-based parameters (M_0, D_0). The computationally-inexpensive thermokinetic grain growth model allowed for a large sample size (N =10,000 simulations) to be used with parameter values chosen randomly within the bounds of -0.5% and +0.5% of the default values. Varying within a set range of percentages essentially normalizes each parameter so that their sensitivities can be prepared. A summary of the grain growth curves is shown in Fig. 9, with the 2%, 10%, and 50% percentile (median) curves shown as a guide to the shape of the distribution. These curves can then be analyzed for their sensitivity with respect to the various Monte Carlo parameters.

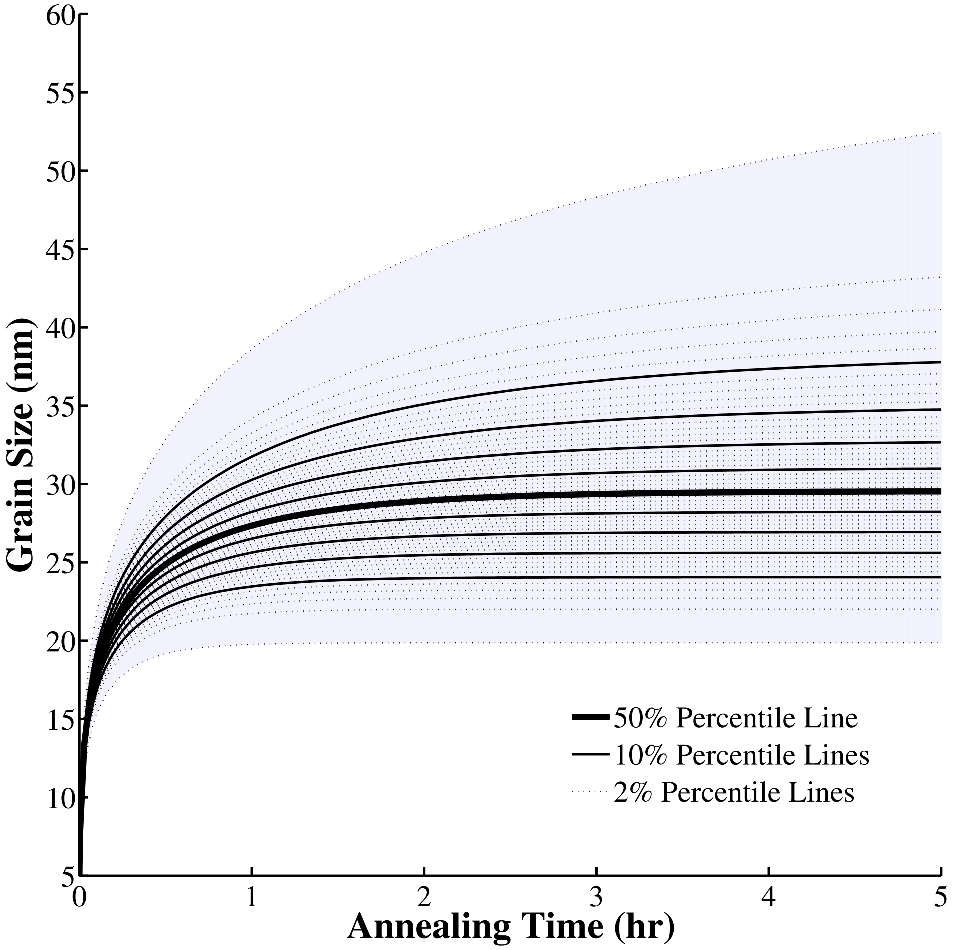

Fig. 9 Grain size evolution as a function of annealing time for the Monte Carlo analysis

Scatter plots are occasionally used to visually examine the correlation between a model parameter and the output. For instance, Fig. 10 shows the scatter in grain size at 1 h as a function of the 4 thermodynamic and kinetic parameters. The red markers represent the 10,000 data points and the line represents the best fit linear regression model for each of the different parameters (without including the other parameters). The spread of the data points indicates the variation as a function of the other parameters — the spread/variation is wider for some of the parameters because they do not account for the variation in the larger effects (higher sensitivity parameters). Another method for examining the correlation between parameters and responses is to perform a rank transformation; in this respect, any nonlinear differences because of the magnitude of the parameter or response changes is removed such that the monotonic nature of the relationships are examined. The rank transformed scatter plot is shown in Fig. 11. In Figs. 10 and 11, H_{seg} has the largest effect (based on slope of the linear regression line), followed by γ_0 and Γ_{b0}, with very little effect from Q_L. Again, the largest effect of Q_L is at shorter times than the 1 h time chosen here, so this effect isn't surprising. The rank transformation shows much wider scatter than the untransformed data.

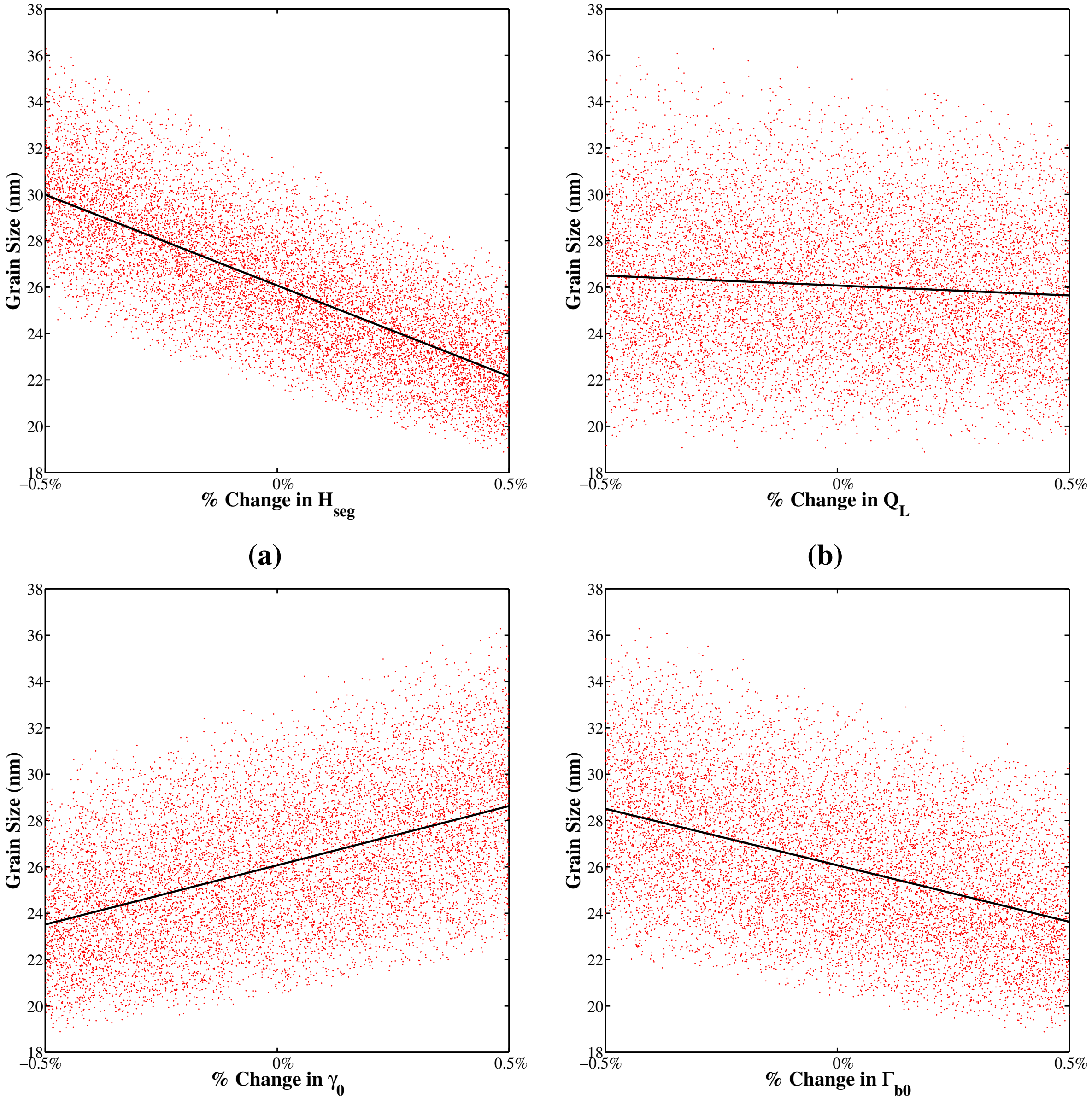

(a) (b)

(c) (d)

Fig. 10 Scatter plot of the grain size as a function of various thermodynamic and kinetic parameters: a) H_{seg}, b) Q_L, c) γ_0, and d) Γ_{b0}. The scatter of the data points is due to the variation in the other parameters at 1 h. The line represents a best fit linear regression model.

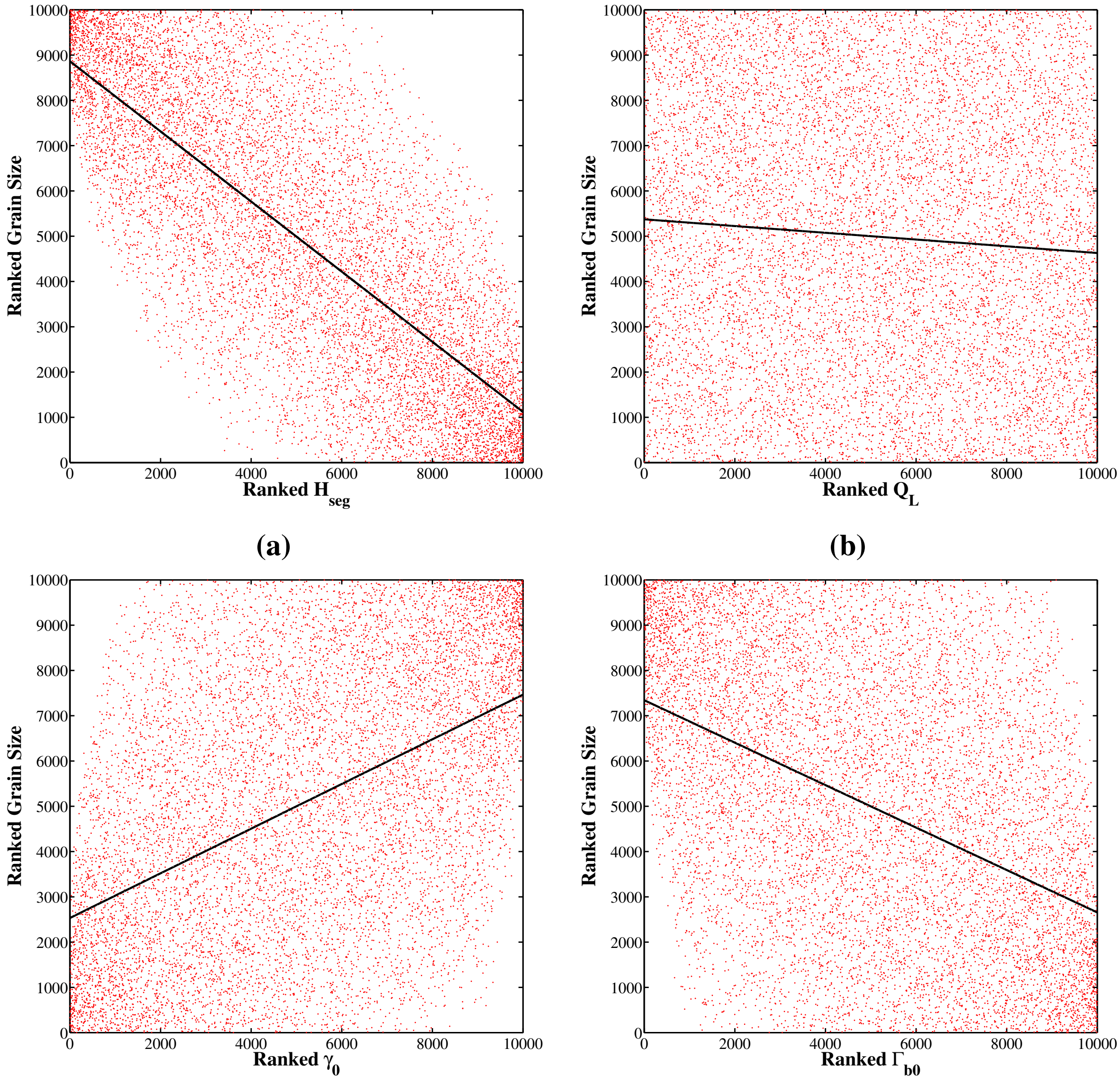

(a) (b)

(c) (d)

Fig. 11 Rank transformation scatter plot of the grain size as a function of thermodynamic and kinetic parameters: a) H_{seg}, b) Q_L, c) γ_0, and d) Γ_{b0}. The scatter of the data points is due to the variation in the other parameters at 1 h. The line represents a best fit linear regression model to the rank transformation data.

In Fig. 12, the correlation coefficient (R) evolution for each of the parameters is plotted as a function of time. This method gives both the direction of the effect and the magnitude of the effect of each parameter. In addition to R, the p-value was also calculated. The parameters M_0 and D_0 were not statistically significant (based on a p-value of 0.05), the activation energy Q_L was only statistically significant for short times ($t \leq\approx 2$ h), and the remaining parameters were statistically significant for all t.

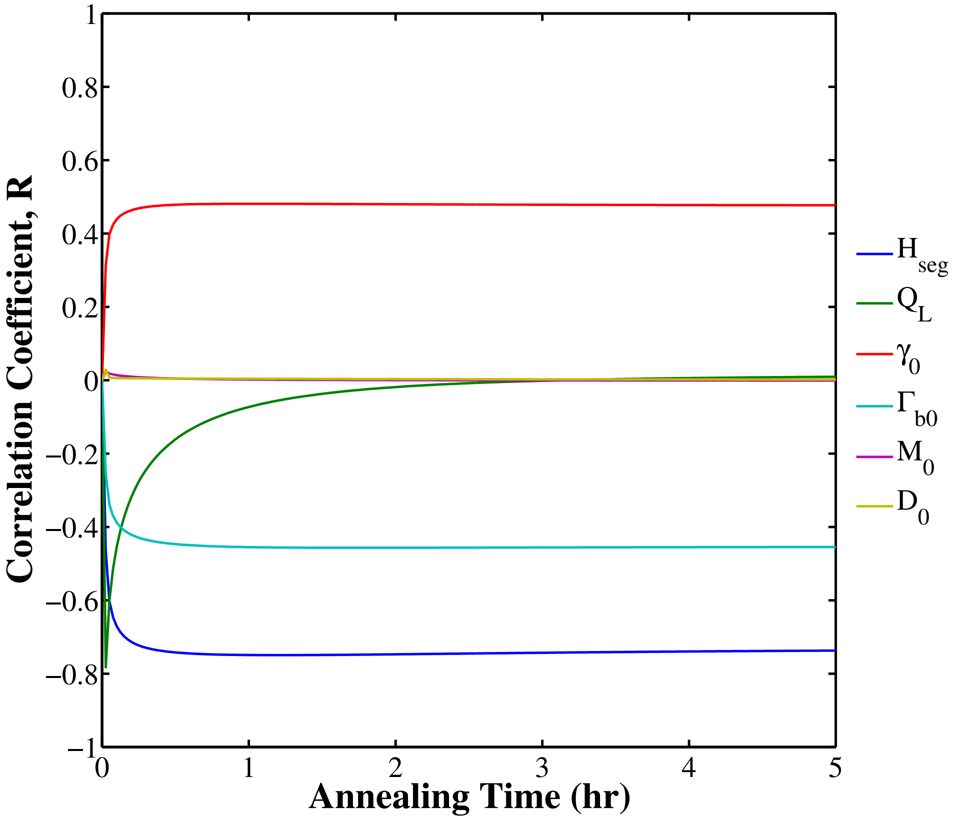

Fig. 12 Evolution of the correlation coefficients as a function of annealing time for the Monte Carlo analysis

The global sensitivity of the 6 parameters can be assessed by fitting the 10,000 grain size evolution curves to the parameters. In this respect, at any time, the output (grain size) $\mathbf{Y}$ can be modeled as a function of the parameters $\mathbf{x}$; i.e., $\mathbf{Y} = f(\mathbf{x}) = f(x_1, x_2, \ldots, x_j)$ where j is the number of parameters. In this respect, the grain size can be modeled by the linear regression model:

$$\mathbf{Y} = C_0 + \sum_{i=1}^{j} C_i \left(\frac{x_i}{x_i^0} - 1 \right), \tag{17}$$

whereby C_0 is the average grain size, C_i is the coefficient (slope) for parameter i, and the final term in the summation normalizes the parameters of x_i by their default value (and subtracts 1) to give a percentage increase or decrease (i.e., normalizing each parameter to be able to compare their effect on grain size C_i). The coefficient C_i is similar to the sensitivity since it is the derivative of the grain size with respect to the percentage increase/decrease. Here, we differentiate the two by taking the absolute value of C_i for a measure of the sensitivity, i.e., $\mathrm{abs}\left(C_i\right)$. In this respect, C_i shows the direction of the parameter effect while $\mathrm{abs}\left(C_i\right)$ shows the degree of sensitivity for comparison of the different parameters.

The evolution of the regression model coefficients is plotted as a function of time to show the sensitivity of the grain size evolution to these parameters. Figure 13 shows the evolution of the regression model coefficients C_i (and the parameter sensitivity) as a function of time. First, Fig. 13a shows the evolution of C_i for each of the parameters as a function of time. The grain boundary energy γ_0 is the only parameter that causes the entire grain size evolution curve to increase with an increase to the parameter (i.e., there is a direct correlation with γ_0). Additionally, the mobility M_0 and initial grain size D_0 have almost no effect and the activation energy Q_L only has an effect at short times. In Fig. 13b, $\mathrm{abs}\left(C_i\right)$ is plotted for the 6 parameters. At very short times, the activation energy Q_L can have as much of an effect as some of the other thermodynamic and kinetic parameters, but this effect decreases as time increases. Moreover, the sensitivity of the heat of segregation H_{seg} is the largest, followed by the grain boundary energy σ_0 and the saturated solute excess Γ_{b0}. However, the evolution of the sensitivity with time is similar for H_{seg}, σ_0, and Γ_{b0}, as is apparent when these parameters are normalized by their maximum sensitivity value (Fig. 13c) and when the evolution of the normalized model coefficient C_i for H_{seg} is compared against that of the other parameters (Fig. 13d). Hence, changes in the parameters H_{seg}, σ_0, and /Γ_{b0} result in a nearly identical effect on the grain size evolution. Clearly, the global sensitivity analysis of Fig. 13 shows that only 2 parameters have independent effects on the thermokinetic model (Q_L and H_{seg}/σ_0/Γ_{b0}).

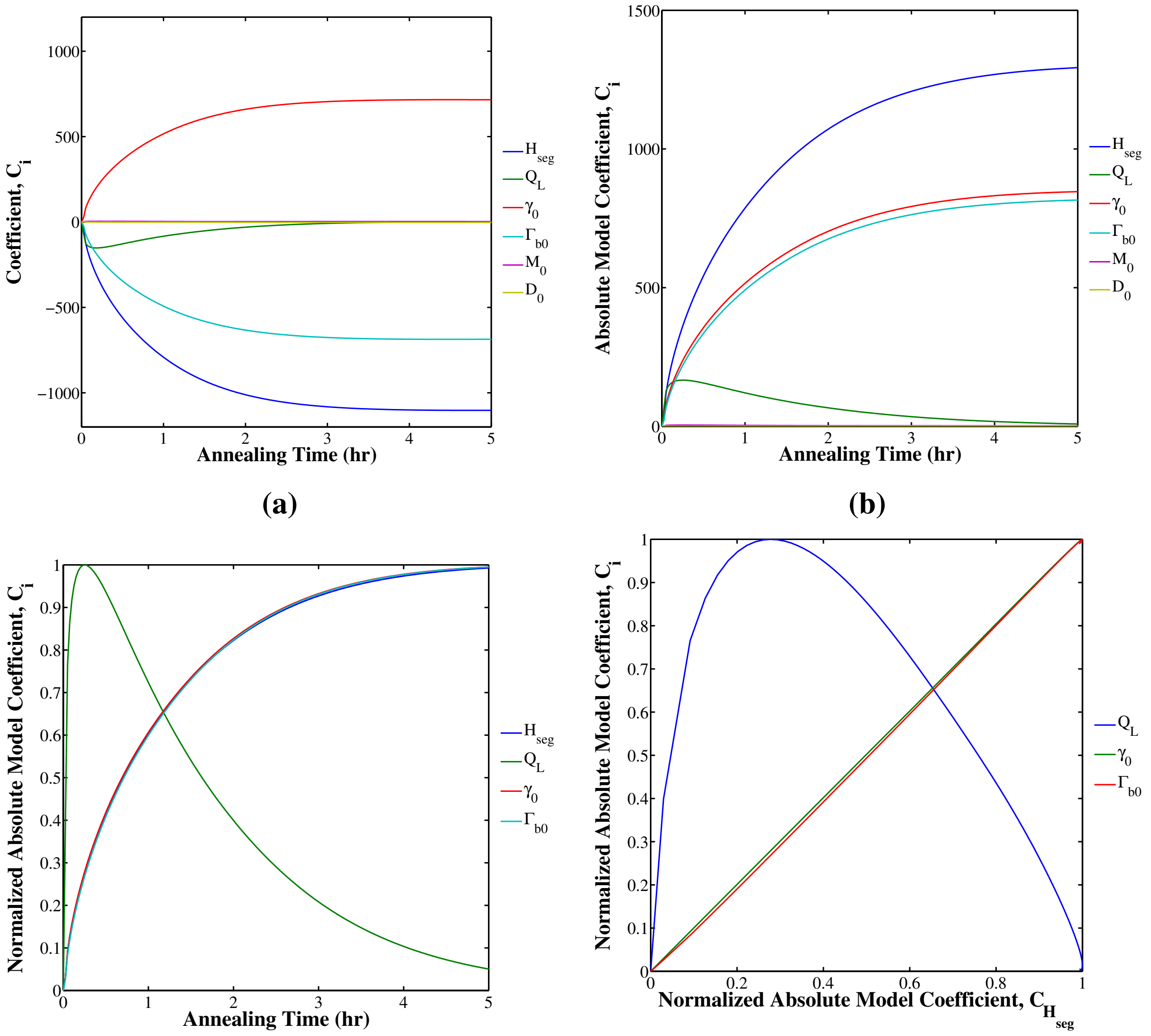

(a) **(b)**

(c) **(d)**

Fig. 13 Grain size sensitivity as a function of annealing time for the Monte Carlo analysis of the different model parameters

There are a few caveats about the present analysis that should be mentioned. First, the 6 parameters explored were each varied by the same percent difference to explore their sensitivity with respect to this difference. In many cases, if the range and distribution of a particular parameter is known and can be measured, this uncertainty can instead be used for the Monte Carlo analysis. As an example, as shown in Fig. 8, certainly M_0 has an effect if it is doubled, but it has no statistical significance if modified by $\pm 0.5\%$ with all other parameters varying by the same percentage. Second, other sensitivity analysis methods were also explored (e.g., the Morris one-at-a-time method) and resulted in similar findings. Furthermore, in varying many of the other material parameters, their effect was also minimal in comparison to the thermodynamic and kinetic parameters of the thermokinetic model.

4.1.3 State Variables: Temperature and Concentration

The change in the grain growth behavior as a function of temperature and concentration is of interest for ultimately tailoring the properties of the nanocrystalline Fe–Zr system. The evolution of the average grain size as a function of different temperatures and concentrations is shown in Fig. 14. Again, the baseline model for nanocrystalline Fe–4% Zr alloy annealed at 800 °C (1,073 K) was used with deviations up to 50 °C and 0.5% Zr concentration. The blue lines represent a lower temperature/concentration (750 °C and 3.5% Zr) and the red lines represent the higher temperature/concentration (850 °C and 4.5% Zr) with intermediate lines shown as well (black dotted lines). Lower temperatures and higher solute concentrations have a smaller stabilized grain size and reach this stabilized grain size much quicker than higher temperatures and lower solute concentrations, as expected. For example, higher solute concentrations at the same temperature means that the GBs can more quickly saturate with solute, thus providing an impediment to further grain growth. While the trends seem appropriate, it should be noted that the magnitude of these changes may not be correct, though. Further data would be needed to validate this behavior as a function of temperature and concentration.

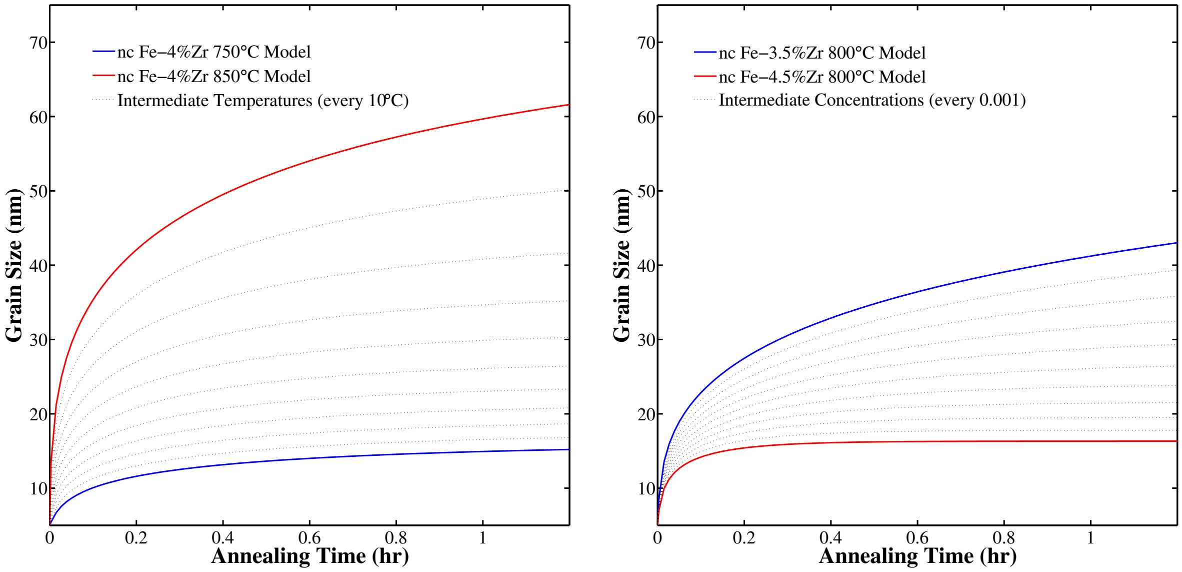

(a) Temperature, T

(b) Concentration, x_0

Fig. 14 Evolution of the average grain size as a function of annealing time for a) nanocrystalline Fe–4% Zr alloy annealed at various temperatures and b) nanocrystalline Fe–Zr alloy with different Zr concentrations annealed at 800 °C (1,073 K)

The thermokinetic model can use these state variables to show potential processing paths that can be used for tailoring the grain size (and properties) of nanocrystalline materials. We developed a thermokinetic stability map as a function of temperature T and solute concentration x_0 (Fig. 15). The thermokinetic stability map fits the present model to the experimental data obtained (Fig. 2) and can then calculate the change in D^* with temperature and concentration. In certain regions, the present model predicts no grain growth and, in other regions, the model predicts no stabilized grain size. However, it should be noted that the present model does not account for changes in the material parameters as a function of temperature and concentration. Present applications of the thermokinetic model have been to fit experimental datasets in both nanocrystalline metal (e.g., Fe–Zr, Ru–Al) and ceramic systems. In truth, extending these models to include the change in material parameters, such as GB energy, with temperature and/or concentration would be beneficial for generating thermokinetic stability maps for processing nanocrystalline materials.

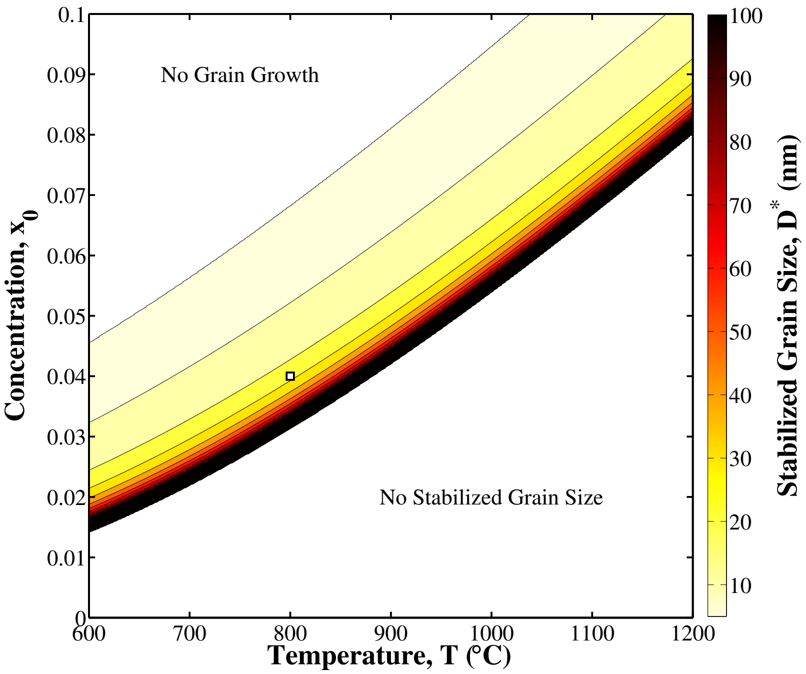

Fig. 15 Thermokinetic stability map of the evolution of the stabilized grain size as a function of temperature T and solute concentration x_0 for the nanocrystalline Fe–Zr system. The white square data point shows the location of the experimental data used for fitting the thermokinetic model (in Fig. 2) for a nanocrystalline Fe–4% Zr alloy annealed at 800 °C (1,073 K).

4.2 Thermokinetic Model Extension

This subsection focuses on extending the present model to handle a wider range of grain growth in nanocrystalline materials. First, the present model is applied to the Fe–4% Zr alloy at the multiple temperatures associated with the XRD data. The optimal material parameters are listed in Table 4 for 3 different cases: 1) all 4 parameters included in optimization, 2) γ_0 is held constant, and 3) both γ_0 and Γ_{b0} are held constant. These 3 cases are separated into blocks within the table. Certain trends emerge based on these optimal parameter sets. In the first case, it can be seen that the GB energy γ_0 is strongly tied to the enthalpy change ΔH_{seg}. Hence, in the second and third cases, the GB energy is held constant to examine the influence of the other parameters. Furthermore, the saturated excess Γ_{b0} was trending in opposite directions with increasing temperature for the first 2 cases so that, in the third case, this parameter was held constant. Interestingly, in all 3 cases, the activation energy Q_L tends to decrease with increasing temperature. Furthermore, when the GB energy is held constant, the enthalpy change decreases. Because the range of applicability of these models is limited (Fig. 14), including the influence of temperature on these material parameters extends the range of applicability for this model. Figure 16 shows examples of the present thermokinetic model, without any extensions, fit to the Fe–Zr grain size data herein.

Table 4 Optimal material parameter sets for Fe–4% Zr

Temperature (°C) T	GB energy ($\mathrm{J\,m^{-2}}$) γ_0	Saturated excess ($10^{-5}\,\mathrm{mol\,m^{-2}}$) Γ_{b0}	Enthalpy change ($\mathrm{kJ\,mol^{-1}}$) ΔH_{seg}	Activation energy ($\mathrm{kJ\,mol^{-1}}$) Q_L
700	0.729	1.243	89.7	337.5
800	0.733	1.228	90.6	332.2
900	0.755	1.159	95.7	324.2
1,000	0.743	1.178	93.6	327.0
700	0.730[a]	1.257	89.2	337.7
800	0.730[a]	1.247	89.6	332.5
900	0.730[a]	1.358	84.6	327.1
1,000	0.730[a]	1.488	80.1	331.5
700	0.730[a]	1.250[a]	89.5	337.5
800	0.730[a]	1.250[a]	89.4	332.5
900	0.730[a]	1.250[a]	89.1	325.6
1,000	0.730[a]	1.250[a]	89.1	328.2

[a] Indicates that this variable was held constant during optimization.

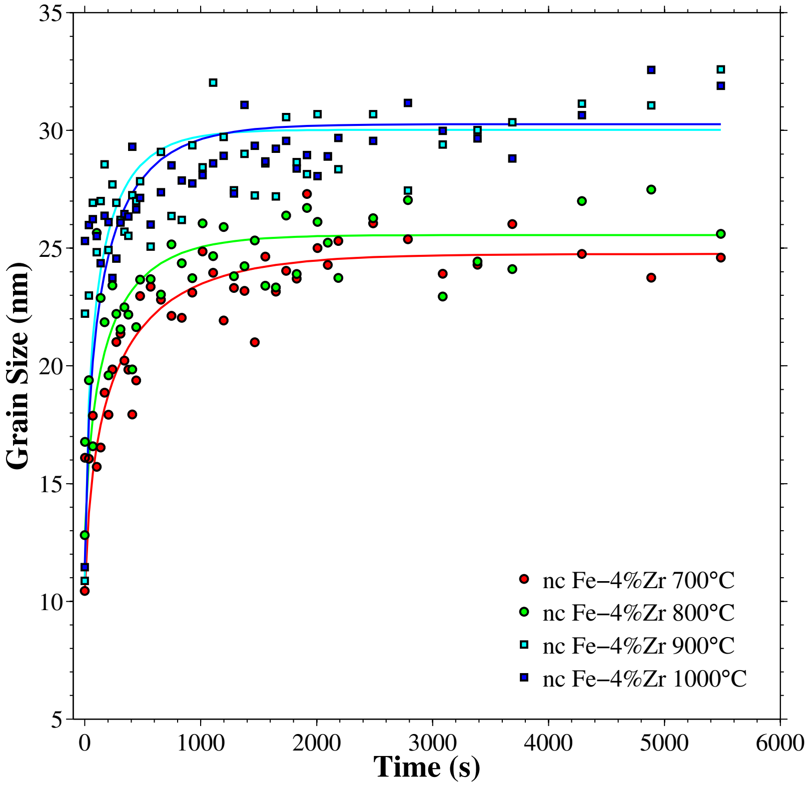

Fig. 16 Evolution of the average grain size as a function of annealing time at multiple temperatures (700–1,000 °C) for nanocrystalline Fe–4% Zr. The lines represent the fit from the thermokinetic model for the various temperatures.

4.2.1 Temperature Dependence

The thermokinetic model was extended by including the dependence of the GB energy γ_0 and activation energy Q_L on temperature (Note that the parameter γ_0 was chosen instead of ΔH_{seg}, because of its similarity to Q_L compare Eqs. 6 and 12). A linear dependence on temperature was assumed for the evolution of GB energy γ_0, which seems reasonable given recently simulated trends in the GB free energy with temperature,[59] i.e.,

$$\gamma_0(T) = \gamma_{0,0} + \gamma_{0,1}T \tag{18}$$

where $\gamma_{0,0}$ is the intercept and $\gamma_{0,1}$ is the slope of γ_0 with respect to temperature. An Arrhenius relation was chosen to represent the temperature dependence of the activation energy Q_L, i.e.,

$$Q_L(T) = Q_{L,0} \exp\left(-\frac{Q_{L,1}}{RT}\right) \tag{19}$$

respectively, where $Q_{L,0}$ is the pre-exponential factor and $Q_{L,1}$ is an exponential constant, respectively. The thermokinetic model with temperature-dependent γ_0 and Q_L was applied to the Fe–4% Zr XRD data and the resulting fit is shown in Fig. 17. The resulting parameters for this model are listed in Table 5 and the calculated values of the material parameters are listed in Table 6. While the overall fit of this model is less accurate than individually fitting each temperature, the general agreement with the experiments is good and the model captures the trend of the experimental data. Furthermore, because γ_0 and Q_L now change as a function of temperature and the fit uses the entire Fe–4% Zr XRD dataset, this allows the model to be extended over a much larger temperature range than the thermokinetic model as applied to experimental data from 1 temperature. Additionally, because of the non-uniqueness of solutions as applied to 1 temperature, applying the models with temperature dependence to the entire range of data can help to obtain unique sets of optimal material parameters. Last, this model was also applied to the Fe–1% Zr case (Fig. 18) and shows reasonable agreement with the experimental XRD data.

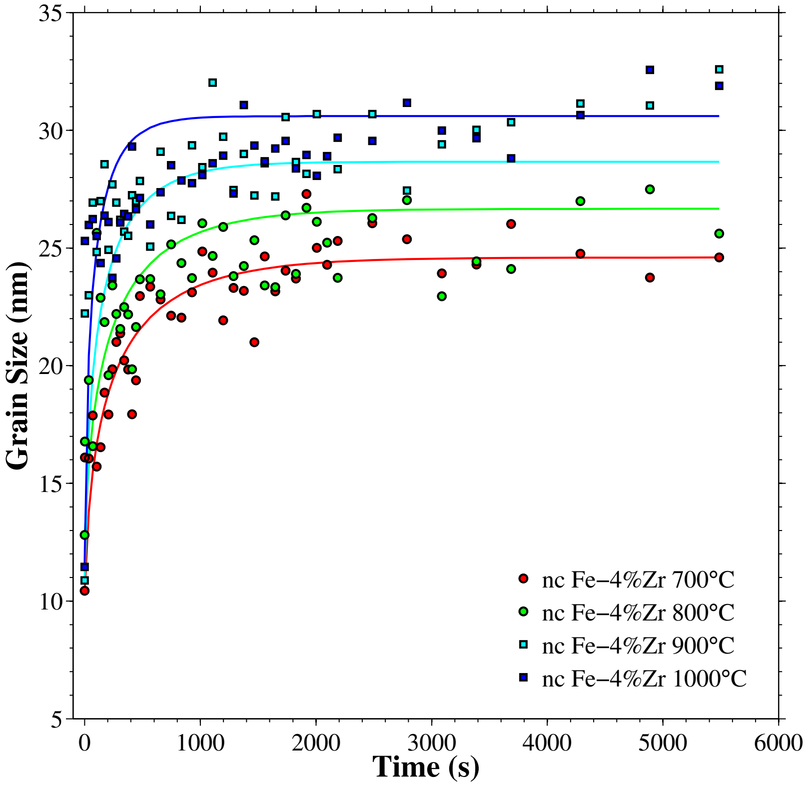

Fig. 17 Evolution of the average grain size as a function of annealing time at multiple temperatures (700–1,000 °C) for nanocrystalline Fe–4% Zr. The lines represent the fit from the thermokinetic model with temperature dependence for γ_0 and Q_L (Eqs. 18 and 19).

Table 5 Optimal temperature-dependent constants for γ_0 and Q_L in modified thermokinetic model for Fe–4% Zr

$\gamma_{0,0}$ ($\mathrm{J\,m^{-2}}$)	$\gamma_{0,1}$ ($\mathrm{J\,m^{-2}\,K^{-1}}$)	$Q_{L,0}$ ($\mathrm{kJ\,mol^{-1}}$)	$Q_{L,1}$ ($\mathrm{kJ\,mol^{-1}}$)
1.227	-3.39×10^{-4}	805	7.85

Table 6 Optimal material parameter sets for Fe–4% Zr in temperature-dependent thermokinetic model (calculated using parameters in Table 5)

Temperature (°C) T	GB energy ($\mathrm{J\,m^{-2}}$) $\gamma_0(T)$	Saturated excess ($10^{-5}\,\mathrm{mol\,m^{-2}}$) Γ_{b0}	Enthalpy change ($\mathrm{kJ\,mol^{-1}}$) ΔH_{seg}	Activation energy ($\mathrm{kJ\,mol^{-1}}$) $Q_L(T)$
700	0.897	1.250[a]	100[a]	305.1
800	0.863	1.250[a]	100[a]	333.9
900	0.829	1.250[a]	100[a]	359.9
1,000	0.795	1.250[a]	100[a]	383.4

[a] Indicates that this variable was held constant during optimization.

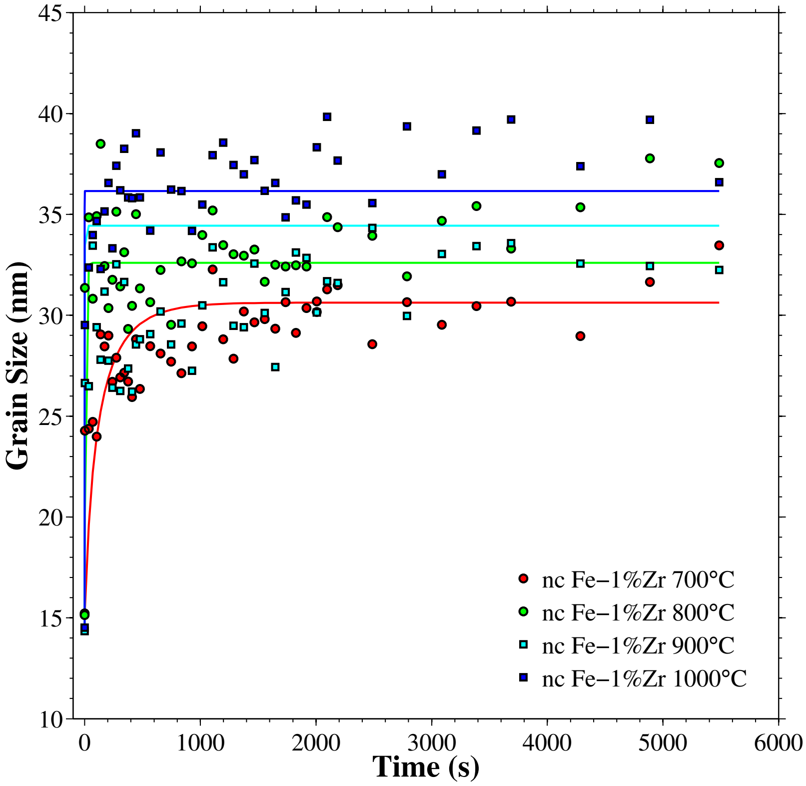

Fig. 18 Evolution of the average grain size as a function of annealing time at multiple temperatures (700–1,000 °C) for nanocrystalline Fe–1% Zr. The lines represent the fit from the thermokinetic model with temperature dependence for γ_0 and Q_L (Eqs. 18 and 19).

Figures 17 and 18 experimentally show that, irrespective of Zr concentration, the average grain size within both samples (1 and 4 at% Zr) increases as the annealing temperature is increased. However, the average grain size for samples containing Fe–4 at% Zr are smaller than in the Fe–1 at% Zr samples at equivalent temperatures. When comparing the 2 sets of data in Figs. 17 and 18, the experimental XRD datasets reveal changes in the kinetics of grain growth. The alloy containing 4 at% Zr shows similar growth rates for all temperatures tested. A steady increase in the average grain size occurs for times up to 1,000 s, after which saturation occurs. The alloy containing 1 at% Zr behaves similarly at 700 °C, but growth above that temperature is nearly instantaneous, reaching saturation within the first 30 s.

4.3 Grain Size Distribution Dependence

It is also important to understand how an initial grain size distribution affects the evolution behavior within the thermokinetic model. In applications of the thermokinetic model, the scalar value for initial grain size represents the average grain size. However, it is well known that most polycrystalline materials have a lognormal distribution of grain sizes. To model the effect of a normal and lognormal grain size distribution, a Monte Carlo analysis is applied to the thermokinetic model, whereby the initial grain size was randomly chosen 1,000 times from these 2 distributions (with a 2 nm standard deviation). Figure 19 shows the results of these calculations for a) a normal distribution and b) a lognormal distribution with the modified temperature-dependent thermokinetic model. In these plots, the shaded regions denote the span of the grain growth curves from these 1,000 samples for each temperature (700, 800, 900, and 1,000 °C). The lines within the distributions denote the median behavior (thick line), the 10th percentiles of the distribution (dashed lines), and the minimum/maximum values of the distribution (bounding lines of shaded region). Interestingly, at short times, the initial grain size distribution rapidly approaches the average grain size behavior d_{ave}. For instance, for smaller grain sizes ($d < d_{ave}$), there is a larger driving force for grain growth. As a result, these grain sizes rapidly converge to the mean behavior. For larger grain sizes ($d > d_{ave}$), there is a smaller driving force for grain growth and so these grain sizes very slowly evolve towards the stabilized grain size. This behavior can also be inferred from the evolution of the standard deviation of these distributions (Fig. 20). Notice that the standard deviation for all temperatures and both distributions starts at 2 nm and rapidly decreases until it reaches a linear regime (on a logarithmic scale, though). So, with respect to Figs. 19 and 20, while the shaded region in Fig. 19 reflects a broad initial grain size distribution, the majority of the distribution rapidly converges to the mean behavior while grain sizes that are far greater than d_{ave} slowly converge. At long times, the initial distribution of grain sizes will approach a single stabilized grain size. These observations are true for both of the distributions.

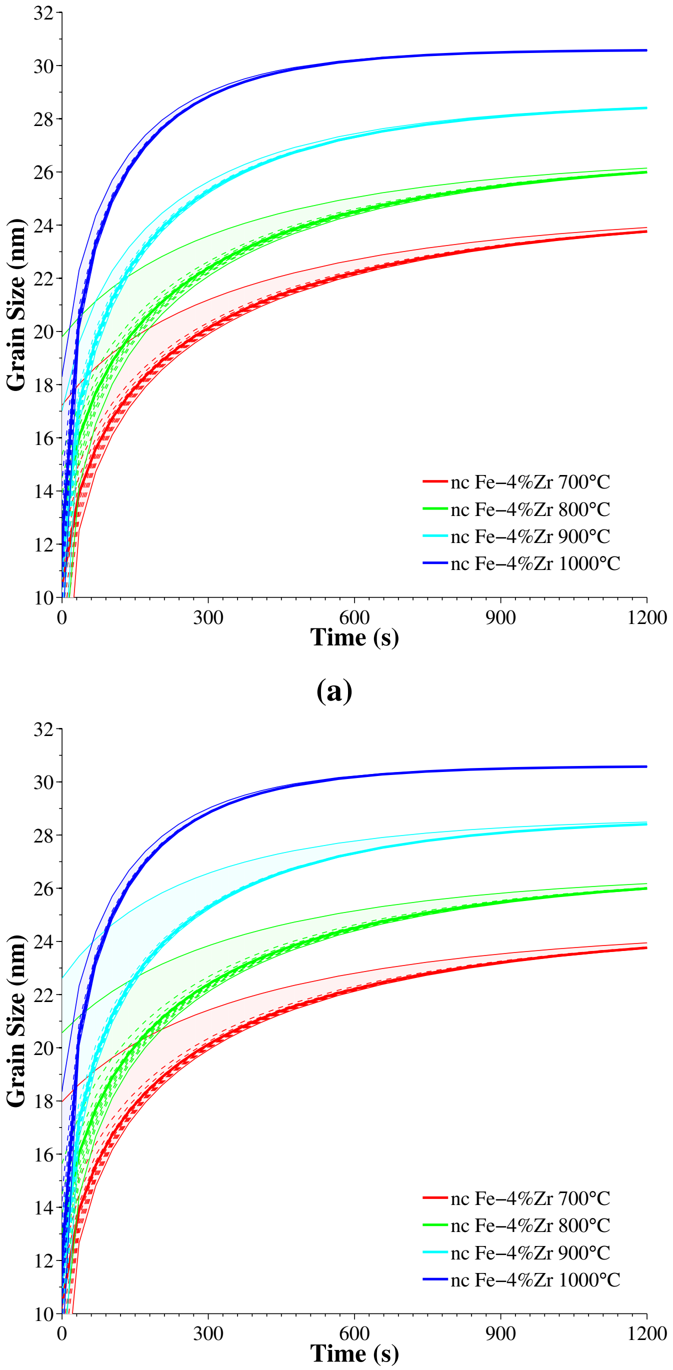

(a)

(b)

Fig. 19 Grain size distribution evolution as a function of annealing time for a) a normal distribution and b) a lognormal distribution. The lines within the distributions denote the median behavior (thick line), the 10th percentiles of the distribution (dashed lines), and the minimum/maximum values of the distribution (bounding lines of shaded region).

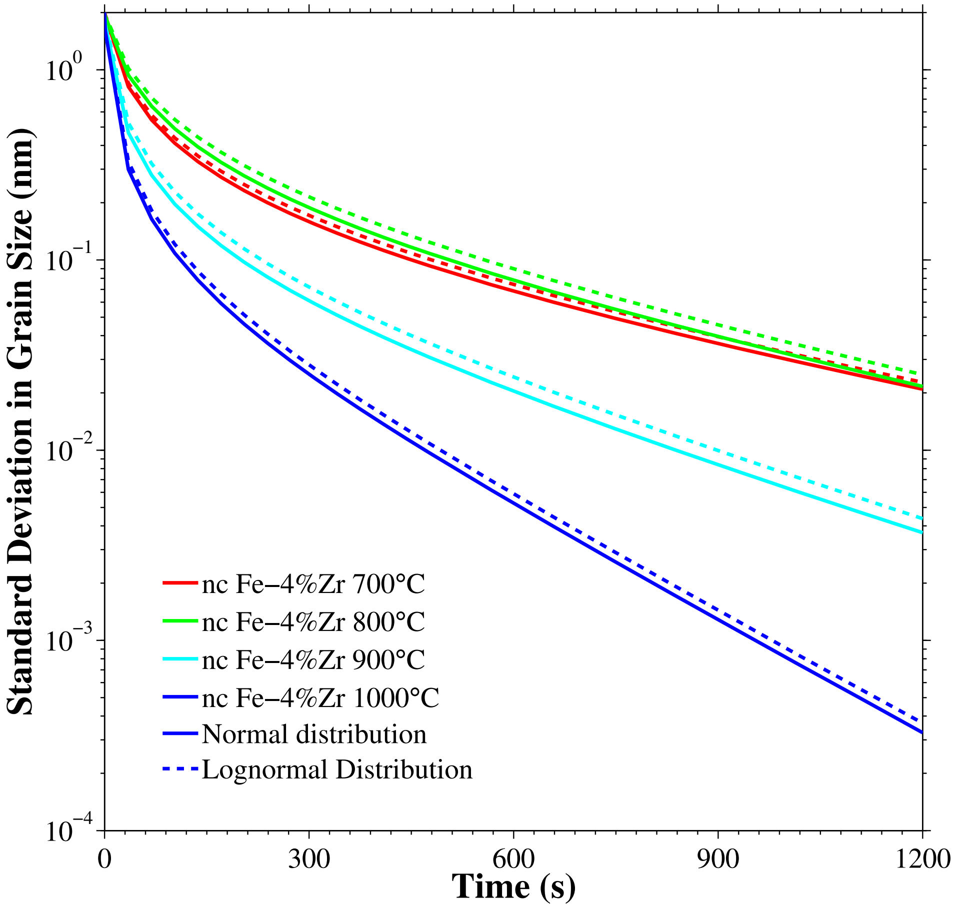

Fig. 20 Evolution of the standard deviation of the grain size distribution as a function of annealing time

5. Discussion

This study examined the thermodynamic and kinetic parameters of the as-formulated thermokinetic model and proposed extensions to the formulation to capture the temperature dependence of grain growth within this model formulation. The present predictive model captures the influence of temperature better than previously-implemented versions of the thermokinetic model, which could only be fit to existing data at a particular temperature and had little predictive capability for grain growth outside of the initial conditions (temperature, concentration, etc.). For example, compare the predictive capability of the original model in Fig. 14 with the predictive capability of the extended model in Figs. 17 and 18. As further illustration of this difference, Fig. 21 shows the thermokinetic model a) with and b) without the temperature dependence in the thermodynamic/kinetic parameters. In the case of the original model (Fig. 21b), the temperature could only be extended ±50 °C from the temperature used to fit the model; the difference in the low and high temperatures (750 and 850 °C, respectively) with this model resulted in a difference in grain size of approximately 400% after 1 h. In the case of the extended model herein (Fig. 21a), the same temperature increase (ΔT =100 °C) shows an increase of approximately 10% in grain size after the same time interval (1 h), in agreement with experimental results. The experimentally-measured XRD data over a 400 °C temperature range is shown as black diamonds in Fig. 21 to illustrate the magnitude of the variation in grain size with a temperature difference that is 4 times that plotted for the models in Fig. 21.

Future extensions could look at extending this thermokinetic model to include concentration dependence as well. In this respect, not only would concentration potentially affect the thermodynamic and kinetic parameters, but a number of material parameters would also be similarly affected. Additionally, concentration dependence may cause problems in regimes where rampant grain growth exists (Fe–0% Zr) or intermetallic formation may become an issue (Fe–10% Zr). Furthermore, there is a lot of inherent noise (and uncertainty) in the XRD measurements. Nondestructive techniques that can dynamically capture the evolution of grain size with time with less uncertainty would certainly improve the predictive capability of the thermokinetic grain growth model. The ability to predict grain growth in nanocrystalline materials based on both thermodynamic and kinetic approaches may better enable high temperature processing and consolidation of these materials.

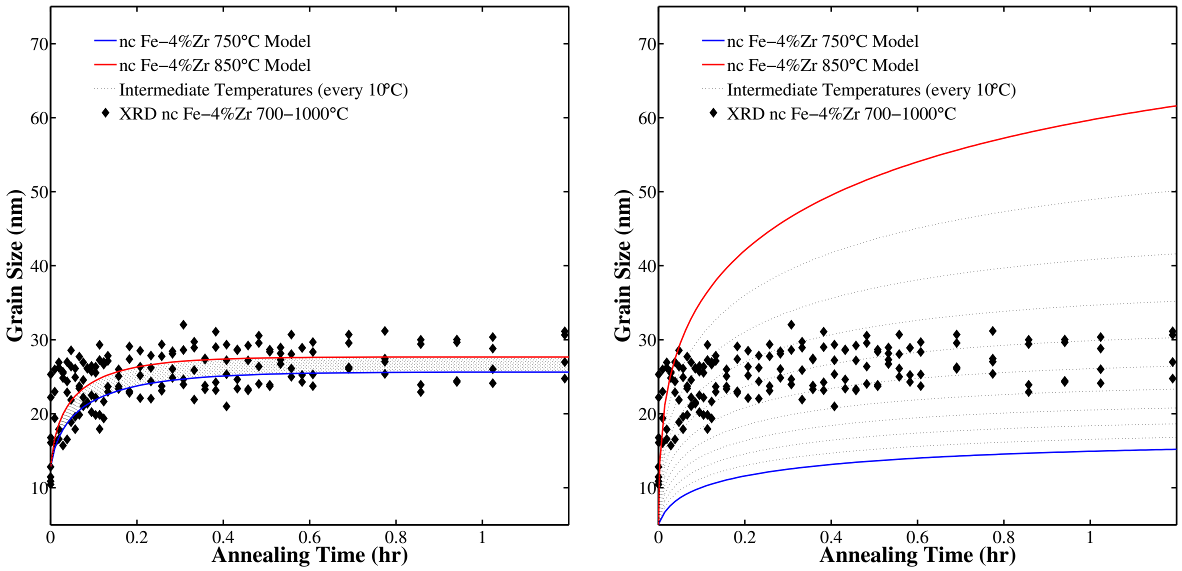

(a) **(b)**

Fig. 21 Evolution of the average grain size as a function of annealing time for nanocrystalline Fe–4% Zr alloy annealed at various temperatures in the range 750–850 °C. Experimentally-measured XRD data for a 400 °C range is shown (black diamonds) along with the thermokinetic model a) with and b) without the temperature dependence.

6. Conclusions

In this work, a thermokinetic model for grain growth was applied to experimental XRD measurements from nanocrystalline Fe–Zr in an effort 1) to understand the influence of thermodynamic, kinetic, and material parameters in the model; and 2) to extend the thermokinetic model by incorporating temperature dependence. The model performs well for the grain boundary saturated case in the nanocrystalline Fe–Zr system, where Zr segregate to the Fe GBs and thermodynamically/kinetically reduce the driving force for grain growth. In this work, a sensitivity analysis of parameters (Monte Carlo global sensitivity analysis with 10,000 instantiations) shows that only 2 independent thermodynamic/kinetic parameters affect the grain size evolution: the activation energy (Q_L) and the heat of segregation/grain boundary energy/grain boundary saturated excess (H_{seg}/γ_0/Γ_{b0}, respectively), whose effects were all highly correlated. Moreover, the predictive capability of the model was examined. After fitting to grain growth at 1 temperature/concentration condition, the model performed poorly at temperatures as close as ±50 °C and concentrations as close as ±0.5 at%. This model was then extended to include the change in 2 independent thermodynamic/kinetic parameters as a function of temperature to model grain growth over a variety of temperatures for the Fe–Zr system, in agreement with the experimental data for the Fe–Zr system. Last, a Monte Carlo analysis explored the effect of grain size distribution and found that the grain size distribution rapidly converged to the mean behavior. At long times, the grain size converged to a single stabilized grain size. The significance of this research is that the thermodynamic and kinetic contributions may be necessary to help explain grain growth in nanocrystalline materials. Furthermore, this model formulation can be extended to understanding how grain size evolves as a function of temperature for other nanocrystalline systems.

7. References

1. Gleiter H. Nanocrystalline materials. Progress in Materials Science. 1989;33(4):223–315.
2. Sanders PG, Eastman JA, Weertman JR. Elastic and tensile behavior of nanocrystalline copper and palladium. Acta Materialia. 1997;45(10):4019–4025.
3. Weertman JR. Hall–Petch strengthening in nanocrystalline metals. Materials Science and Engineering A. 1993;166(1–2):161–167.
4. Nieman GW, Weertman JR, Siegel RW. Mechanical behavior of nanocrystalline Cu and Pd. Journal of Materials Research. 1991;6(5):1012–1027.
5. Nieh TG, Wadsworth J. Hall–Petch relation in nanocrystalline solids. Scripta Metallurgica Et Materialia. 1991;25(4):955–958.
6. Kumar KS, Van Swygenhoven H, Suresh S. Mechanical behavior of nanocrystalline metals and alloys. Acta Materialia. 2003;51(19):5743–5774.
7. Meyers MA, Mishra A, Benson DJ. Mechanical properties of nanocrystalline materials. Progress in Materials Science. 2006;51(4):427–556.
8. Lu L, Shen YF, Chen XH, Qian LH, Lu K. Ultrahigh strength and high electrical conductivity in copper. Science. 2004;304(5669):422–426.
9. Hall EO. The deformation and ageing of mild steel III. Discussion of results. Proceedings of the Physical Society of London Section B. 1951;64(381):747–753.
10. Petch NJ. The cleavage strength of polycrystals. Journal of the Iron and Steel Institute. 1953;174(1):25–28.
11. Atwater MA, Bahmanpour H, Scattergood RO, Koch CC. The thermal stability of nanocrystalline cartridge brass and the effect of zirconium additions. Journal of Materials Science. 2013;48(1):220–226.
12. Atwater MA, Roy D, Darling KA, Butler BG, Scattergood RO, Koch CC. The thermal stability of nanocrystalline copper cryogenically milled with tungsten. Materials Science and Engineering A. 2012;558(0):226–233.

13. Atwater MA, Scattergood RO, Koch CC. The stabilization of nanocrystalline copper by zirconium. Materials Science and Engineering A. 2013;559:250–256.

14. Darling KA, Chan RN, Wong PZ, Semones JE, Scattergood RO, Koch CC. Grain-size stabilization in nanocrystalline FeZr alloys. Scripta Materialia. 2008;59(5):530–533.

15. Darling KA, Guduru RK, Reynolds CL, Bhosle VM, Chan RN, Scattergood RO, Koch CC, Naravan J, Aboelfotoh MO. Thermal stability, mechanical and electrical properties of nanocrystalline Cu_3Ge. Intermetallics. 2008;16(3):378–383.

16. Darling KA, VanLeeuwen BK, Koch CC, Scattergood RO. Thermal stability of nanocrystalline Fe-Zr alloys. Materials Science and Engineering A. 2010;527(15):3572–3580.

17. Makino A, Bitoh T. High coercivity of melt-spun $(Fe_{0.55}Pt_{0.45})_{(78)}Zr_{2-4}B_{18-20}$ nanocrystalline alloys with $L1_{(0)}$ structure. Journal of Applied Physics. 2004;95(11):7498–7500.

18. Talin AA, Marquis EA, Goods SH, Kelly JJ, Miller MK. Thermal stability of Ni-Mn electrodeposits. Acta Materialia. 2006;54(7):1935–1947.

19. Thuvander M, Abraham M, Cerezo A, Smith GDW. Thermal stability of electrodeposited nanocrystalline nickel and iron-nickel alloys. Materials Science and Technology. 2001;17(8):961–970.

20. Detor AJ, Schuh CA. Grain boundary segregation, chemical ordering and stability of nanocrystalline alloys: Atomistic computer simulations in the Ni-W system. Acta Materialia. 2007;55(12):4221–4232.

21. Aust KT, Hibbard G, Palumbo G, Erb U. Intercrystalline defects and some properties of electrodeposited nanocrystalline nickel and its alloys. Zeitschrift Für Metallkunde. 2003;94(10):1066–1072.

22. Chen Z, Liu F, Yang XQ, Shen CJ. A thermokinetic description of nanoscale grain growth: Analysis of the activation energy effect. Acta Materialia. 2012;60(12):4833–4844.

23. Chen Z, Liu F, Zhang K, Ma YZ, Yang GC, Zhou YH. Description of grain growth in metastable materials prepared by non-equilibrium solidification. Journal of Crystal Growth. 2010;313(1):81–93.

24. Frolov T, Darling KA, Kecskes LJ, Mishin Y. Stabilization and strengthening of nanocrystalline copper by alloying with tantalum. Acta Materialia. 2012;60(5):2158–2168.

25. Gong MM, Liu F, Zhang K. Thermodynamic stability of binary nanocrystalline alloys: Analysis of solute and excess vacancy. Applied Physics A. 2011;105(4):927–934.

26. Millett PC, Selvam RP, Saxena A. Stabilizing nanocrystalline materials with dopants. Acta Materialia. 2007;55(7):2329–2336.

27. Murdoch HA, Schuh CA. Stability of binary nanocrystalline alloys against grain growth and phase separation. Acta Materialia. 2013;61(6):2121–2132.

28. Rajgarhia RK, Koh SW, Spearot D, Saxena A. Microstructure stability of nanocrystalline materials using dopants. Molecular Simulation. 2008;34(1):35–40.

29. Rajgarhia RK, Saxena A, Spearot DE, Hartwig KT, More KL, Kenik EA, Meyer H. Microstructural stability of copper with antimony dopants at grain boundaries: Experiments and molecular dynamics simulations. Journal of Materials Science. 2010;45(24):6707–6718.

30. Saber M, Kotan H, Koch CC, Scattergood RO. Thermal stability of nanocrystalline Fe-Cr alloys with Zr additions. Materials Science and Engineering A. 2012;556:664–670.

31. Saber M, Kotan H, Koch CC, Scattergood RO. Thermodynamic stabilization of nanocrystalline binary alloys. Journal of Applied Physics. 2013;113(6):063515.

32. Trelewicz JR, Schuh CA. Grain boundary segregation and thermodynamically stable binary nanocrystalline alloys. Physical Review B. 2009;79(9).

33. Ames M, Markmann J, Karos R, Michels A, Tschope A, Birringer R. Unraveling the nature of room temperature grain growth in nanocrystalline materials. Acta Materialia. 2008;56(16):4255–4266.

34. Suryanarayana C. Mechanical alloying and milling. Progress in Materials Science. 2001;46(1–2):1–184.

35. Suryanarayana C, Ivanov E, Boldyrev VV. The science and technology of mechanical alloying. Materials Science and Engineering A. 2001;304–306(0):151–158.

36. Detor AJ, Miller MK, Schuh CA. Solute distribution in nanocrystalline Ni-W alloys examined through atom probe tomography. Philosophical Magazine. 2006;86(28):4459–4475.

37. Detor AJ, Miller MK, Schuh CA. Measuring grain-boundary segregation in nanocrystalline alloys: Direct validation of statistical techniques using atom probe tomography. Philosophical Magazine Letters. 2007;87(8):581–587.

38. Koch CC, Scattergood RO, Darling KA, Semones JE. Stabilization of nanocrystalline grain sizes by solute additions. Journal of Materials Science. 2008;43(23–24):7264–7272.

39. Kirchheim R. Grain coarsening inhibited by solute segregation. Acta Materialia. 2002;50(2):413–419.

40. Cahn JW. Impurity-drag effect in grain boundary motion. Acta Metallurgica. 1962;10:789.

41. Nes E, Ryum N, Hunderi O. On the Zener drag. Acta Metallurgica. 1985;33(1):11–22.

42. Chen Z, Liu F, Wang HF, Yang W, Yang GC, Zhou YH. A thermokinetic description for grain growth in nanocrystalline materials. Acta Materialia. 2009;57(5):1466–1475.

43. Gong MM, Liu F, Zhang K. A thermokinetic description of nanoscale grain growth: Analysis of initial grain boundary excess amount. Scripta Materialia. 2010;63(10):989–992.

44. Vooijs SI, Van Leeuwen Y, Sietsma J, Van derZwaag S. On the mobility of the austenite-ferrite interface in Fe-Co and Fe-Cu. Metallurgical and Materials Transactions A. 2000;31(2):379–385.

45. Borisov VT, Golikov VM, Scherbendiskiy GV. About relation of the diffusion coefficients with the grain boundary energy (in russian). Fizika Metallov I Metallovedeniye. 1964;17:881.

46. Burke JE, Turnbull D. Recrystallization and grain growth. Progress in Metal Physics. 1952;3:220–292.

47. Lagarias JC, Reeds JA, Wright MH, Wright PE. Convergence properties of the Nelder-Mead simplex method in low dimensions. SIAM Journal on Optimization. 1998;9(1):112–147.

48. Koch CC. Synthesis of nanostructured materials by mechanical milling: Problems and opportunities. Nanostructured Materials. 1997;9(1–8):13–22.

49. Fecht HJ. Nanostructure formation by mechanical attrition. Nanostructured Materials. 1995;6(1–4):33–42.

50. Humphreys F, Hatherly M. Recrystallization and Related Annealing Phenomena. Tarrytown (NJ), Elsevier Science: 1996.

51. Streitenberger P. Analytic model of grain growth based on a generalized LS stability argument and topological relationships. Recrystallization and Grain Growth. 2001;1–2:257–262.

52. Wynblatt P, Chatain D. Anisotropy of segregation at grain boundaries and surfaces. Metallurgical and Materials Transactions A. 2006;37A(9):2595–2620.

53. Darling KA, VanLeeuwen BK, Semones JE, Koch CC, Scattergood RO, Kecskes LJ, Mathaudhu SN. Stabilized nanocrystalline iron-based alloys: Guiding efforts in alloy selection. Materials Science and Engineering A 2011;528(13–14):4365–4371.

54. Cullity S, Stock B. Elements of X-Ray Diffraction. Upper Saddle River (NJ): 2001.

55. Chen YZ, Herz A, Kirchheim R. Grain boundary segregation of carbon and formation of nanocrystalline iron-carbon alloys by ball milling. Materials Science Forum. 2010;667–669:265–270.

56. Chen YZ, Herz A, Li YJ, Borchers C, Choi P, Raabe D, Kirchheim R. Nanocrystalline Fe–C alloys produced by ball milling of iron and graphite. Acta Materialia. 2013;61(9):3172–3185.

57. Kotan H, Darling KA, Saber M, Scattergood RO, Koch CC. An in situ experimental study of grain growth in a nanocrystalline $Fe_{91}Ni_8Zr_1$ alloy. Journal of Materials Science. 2013;48(5):2251–2257.

58. Dake JM, Krill CE. Sudden loss of thermal stability in Fe-based nanocrystalline alloys. Scripta Materialia. 2012;66(6):390–393.

59. Foiles SM. Temperature dependence of grain boundary free energy and elastic constants. Scripta Materialia. 2010;62(5):231–234.

INTENTIONALLY LEFT BLANK.

Appendix A. Thermokinetic Model Validation MATLAB Script

This appendix appears in its original form, without editorial change.

```
%% Thermokinetic Grain Growth Model
% ----------------------------------
% Mark Tschopp, U.S. Army Research Laboratory, 2013-2014
% Email: mark.a.tschopp@us.army.mil
%
% The thermokinetic grain growth model is based on Reference [1] by Chen
% and colleagues.  This is the basic implementation of the model from this
% publication.  A basic root finding method is used to calculate the grain
% size as a function of time for this analytical model.
%
% Reference:
% [1] Chen, Liu, Yang, Shen, Acta Materialia, 60 (2012) 4833.

% Clear everything
clear all, close all

% Initialize constants
R = 8.3145;                      % J/mol K; ideal gas constant
V_m =  7.1/(100^3);              % m3 mol-1; Molar volume
M_0 = 0.8;                       % m mol s-1 J-1; Mobility [1]

% Fitted values:
sigma_0 = 0.73;                  % J m-2; Grain boundary energy
H_seg = 89.3*1000;               % J mol-1; Heat of segregation
gamma_b0 =  1.25*10^(-5);        % mol m-2; Saturated solute excess
Q_L = 345.1*1000;                % J mol-1; Activation energy (lattice diffusion)

% State variables
T =  1073;                       % K; Temperature
x_0 =  0.04;                     % Zr Concentration
D_0 =  5*10^(-9);                % m; initial grain size

% Assumptions
gamma_b = 1*gamma_b0;            % =gamma_b0 for saturated case; solute excess
D_D0 = 1;                        % interface diffusion
D_L0 = 1;                        % lattice diffusion (ratio gets used)
D = D_0;

%% Grain Growth Thermodynamics
% These are equations 13 and 14 [1] for the saturated grain boundary case

sigma_1 = sigma_0 - gamma_b0*(R*T*(log(x_0))+H_seg);
sigma_2 = 3*gamma_b0^2*R*T*V_m/x_0;
```

```
sigma_b = sigma_1 + sigma_2*(1/D);

disp(['Sigma_1: ' num2str(sigma_1) ' J/m^2'])
disp(['Sigma_2: ' num2str(sigma_2) ' J/m'])
disp(['Sigma_b: ' num2str(sigma_b) ' J/m^2'])

%% Grian Growth Kinetics
% These are equations 20 and 21 [1] for the saturated grain boundary case

Q_1 = Q_L + R*T*log(D_D0/D_L0)-sigma_0/gamma_b0 + (R*T*(log(x_0))+H_seg);
Q_2 = 3*R*T*V_m*gamma_b0/x_0;
Q_D = Q_1-Q_2/D;

disp(['Q_1: ' num2str(Q_1) ' J/mol'])
disp(['Q_2: ' num2str(Q_2) ' J*m/mol'])
disp(['Q_D: ' num2str(Q_D) ' J/mol'])

%% Stabilization of Nanocrystalline alloys
% Stabilization of grain growth will occur when GBs are saturated and there
% is a negligible difference between $Q_L$ and $Q_D$.  This calculation for
% D_star shows that the stabilized grain size can be calculated even before
% the "path" to the stability is calculated.  Note that negative D_star
% will cause problems with the model.

D_star = -sigma_2/sigma_1;

disp(['D_star: ' num2str(D_star*10^9) ' nm'])

%% Implementation of Thermokinetic Grain Growth Model
% This section implements the thermokinetic grain growth model (equation 24
% from [1]) by using a bisection root finding method to solve for the grain
% size, d, at time t.

% Insert the experimental data
t_exp = [60 15 10 7.5 2.5 0] * 60;          % s; annealing time
D_exp = [26.5 20.5 21.3 19.5 14.3 7.4];     % m; grain size (experimental)

% To match Figure 3 in [1], the end time is set to 1.2 hr
t_end = 1.2*60*60;                          % End time (in seconds)
t_a = []; D_t = [];
count = 1;
t_a(count) = 0; D_t(count) = D_0*10^9;      % Initialize time and grain size
```

```
% Main loop that uses numerical root finding technique to solve the
% analytical thermokinetic expression
for t = 10:t_end/100:t_end % s

    count = count + 1;
    xTol = 0.001e-10;
    xLower = D_0; xUpper = D_star;
    LHS = 0.5*((xLower+sigma_2/sigma_1)^2-(D_0+sigma_2/sigma_1)^2)-...
    (Q_2/(R*T)+2*sigma_2/sigma_1)*(xLower-D_0)+...
    (sigma_2^2/sigma_1^2+sigma_2/sigma_1*Q_2/(R*T)+1/2*(Q_2/(R*T))^2)*...
    log((sigma_1*xLower+sigma_2)/(sigma_1*D_0+sigma_2)); %
    RHS = sigma_1*M_0*exp(-Q_1/(R*T))*t;
    diff_S = LHS-RHS;
    yLower = diff_S;

    xMid = (xLower + xUpper)/2.0;
    LHS = 0.5*((xMid+sigma_2/sigma_1)^2-(D_0+sigma_2/sigma_1)^2)-...
    (Q_2/(R*T)+2*sigma_2/sigma_1)*(xMid-D_0)+...
    (sigma_2^2/sigma_1^2+sigma_2/sigma_1*Q_2/(R*T)+1/2*(Q_2/(R*T))^2)*...
    log((sigma_1*xMid+sigma_2)/(sigma_1*D_0+sigma_2)); %
    RHS = sigma_1*M_0*exp(-Q_1/(R*T))*t;
    diff_S = LHS-RHS;
    yMid = diff_S;

    % Calculate left-hand-side (LHS) and right-hand-side (RHS) of equation
    % and iteratively hone in on the grain size solution (xMid).
    while (xUpper - xLower)/2.0 > xTol
        if yLower * yMid > 0.0
            xLower = xMid;
        else
            xUpper = xMid;
        end
        xMid = (xLower + xUpper)/2.0;
        LHS = 0.5*((xMid+sigma_2/sigma_1)^2-(D_0+sigma_2/sigma_1)^2)-...
        (Q_2/(R*T)+2*sigma_2/sigma_1)*(xMid-D_0)+...
        (sigma_2^2/sigma_1^2+sigma_2/sigma_1*Q_2/(R*T)+1/2*(Q_2/(R*T))^2)*...
        log((sigma_1*xMid+sigma_2)/(sigma_1*D_0+sigma_2));  % Calculate LHS
        RHS = sigma_1*M_0*exp(-Q_1/(R*T))*t;                % Calculate RHS
        diff_S = LHS-RHS;
        yMid = diff_S;
    end

    if xMid > D_star, xMid = D_star; end
```

```
    t_a(count) = t;  D_t(count) = xMid*10^9;

end

%% Plot the results

% Plot the experimental data
plot(t_exp/3600,D_exp,'db','MarkerFaceColor','b'), hold on
xlim([0 1.2])

% Plot the thermokinetic model data
plot(t_a/3600,D_t,'-b','LineWidth',2)

axis square
legend('Fe-Zr Expt','Thermokinetic Model','Location',[0.71 0.2 0.01 0.01]);
xlabel('Annealing Time (hr)',...
    'FontSize',30, 'FontName','Times', 'FontWeight','b');
ylabel('Grain Size (nm)',...
    'FontSize',30, 'FontName','Times', 'FontWeight','b');
set(gca, 'FontSize',24, 'FontName','Times', 'LineWidth',2);
set(get(gca,'Children'),'MarkerSize',10);
axis([0 1.2 5 30])

xlabel(get(get(gca,'xlabel'),'String'), 'FontSize',30, 'FontName','Times',...
    'FontWeight','b');
ylabel(get(get(gca,'ylabel'),'String'), 'FontSize',30, 'FontName','Times',...
    'FontWeight','b');
set(gca, 'FontSize',24, 'FontName','Times', 'LineWidth',2);
title('remove')
legend('boxoff')
axis square
set(gcf,'Position',[1 1 1200 1200])
```

INTENTIONALLY LEFT BLANK.

Appendix B. Thermokinetic Model Optimization MATLAB Script

This appendix appears in its original form, without editorial change.

```
%% Thermokinetic Grain Growth Model
% ---------------------------------
% Mark Tschopp, U.S. Army Research Laboratory, 2013-2014
% Email: mark.a.tschopp@us.army.mil
%
% The thermokinetic grain growth model is based on Reference [1] by Chen
% and colleagues.
%
% Reference:
% [1] Chen, Liu, Yang, Shen, Acta Materialia, 60 (2012) 4833.
%
% In this code, the Fe-4%Zr data is used and the optimization routine is
% outlined for the modified thermokinetic model with temperature dependence
% of thermodynamic/kinetic parameters.  This is performed in a series of
% optimization routines, to ensure convergence of the model.

% Clear everything
clear all, close all

% Import data from Excel file
filename = 'Fe Zr hot XRD complete data set.xls';
[num,txt,raw] = xlsread(filename);

% `inc' specifies which dataset to use, i.e., in this case it is the 4%Zr
% and 700, 800, 900, and 1000 degrees Celsius
inc = [0 0 0 0, 0 0 0 0, 0 0 0 0, 1 1 1 1, 0 0 0 0];
temp = [400 500 600 700, 700 800 900 1000, 700 800 900 1000, ...
    700 800 900 1000, 700 800 900 1000]+273;
conc = [0 0 0 0, 0.005 0.005 0.005 0.005,  0.01 0.01 0.01 0.01, ...
    0.04 0.04 0.04 0.04, 0.1 0.1 0.1 0.1];

% Material parameters
R = 8.3145;                 % J/mol K; ideal gas constant
V_m =  7.1/(100^3);         % m3 mol-1; Molar volume

% Use these two independent thermodynamic/thermokinetic parameters
hseg = zeros(size(inc));
ql = zeros(size(inc));

%% Optimization I
% In this optimization, we are solving for the optimal sigma_0 and Q_L

icount = 0;
```

```
f = 0;
for i = 1:2:39
    imod = (i+1)/2;
    if inc(imod)
        icount = icount + 1;
        t_exp1(:,icount) = num(:,i);
        D_exp1(:,icount) = num(:,i+1)';
        Temp(icount) = temp(imod);
        Conc(icount) = conc(imod);
        T = temp(imod); x_0 = conc(imod);
        t_exp = num(:,i); D_exp = num(:,i+1)';

        % Select starting values
        sigma_0 = 0.73;             % J m-2;
        H_seg = 100*1000;           % J mol-1; Heat of segregation
        gamma_b0 =  1.25*10^(-5);   % mol m-2; saturated solute excess
        Q_L = 345.1*1000;           % J mol-1; lattice diffusion
                                    % activation energy

        save('objfun_mod_exp_sigma0.mat','t_exp','D_exp','T','x_0',...
            'H_seg','gamma_b0');
        x0 = [sigma_0 Q_L];
        options = optimset('Display','off');
        xsol = fminsearch(@objfun_mod_sigma0,x0,options);

        sigma_0 = xsol(1); % J mol-1; Heat of segregation
        Q_L = xsol(2); % J mol-1; lattice diffusion activation energy

        disp(['xsol(1): ' num2str(xsol(1))])
        disp(['xsol(2): ' num2str(xsol(2))])
        f = f + objfun_mod_sigma0(xsol);

        sigma0(imod) = xsol(1);
        ql(imod) = xsol(2);

        % Are initial parameters giving a positive D_star?
        sigma_1 = sigma_0 - gamma_b0*(R*T*(log(x_0))+H_seg);
        sigma_2 = 3*gamma_b0^2*R*T*V_m/x_0;
        D_star = -sigma_2/sigma_1;

        if D_star < 0, stop; end
    end
end
```

```
% `f' is a measure of the goodness of the model fit, e.g., a root mean
% square error or the like
disp(['f: ' num2str(objfun_mod_sigma0(xsol))])

%% Optimization II
% Now use sigma_0 to get good estimates of what the constants describing
% the temperature dependence are.  In this case, Q_L is constant.

n = find(logical(inc));
sigma_0_c1 = mean((sigma0(n(2:end)) - sigma0(n(1)))./temp(n(2:end)));
sigma_0_c0 = sigma0(n(1)) - sigma_0_c1*temp(n(1));

Q_L = mean(ql(n));

save('objfun_mod2_exp_sigma0.mat','t_exp1','D_exp1','Temp','Conc',...
    'H_seg','gamma_b0', 'Q_L');
x0 = [sigma_0_c0 sigma_0_c1];
options = optimset('Display','off');
xsol = fminsearch(@objfun_mod2_sigma0,x0,options);

disp(['xsol(1): ' num2str(xsol(1))])
disp(['xsol(2): ' num2str(xsol(2))])

sigma_0_c0 = xsol(1);
sigma_0_c1 = xsol(2);

disp(['f: ' num2str(objfun_mod2_sigma0(xsol))])

%% Optimization III
% Now use Q_L to get good estimates of what the constants describing
% the temperature dependence are.  In this case, sigma_0 is constant.  In
% this routine, multiple starting positions are utilized to find the
% minimum error solution to the thermokinetic equations.

Q_L_c0 = Q_L; Q_L_c1 = 1;
best = 100;

for i = 0.7:0.1:1.3
    for j = 0:0.5:5
        Q_L_c0 = i*Q_L;
        Q_L_c1 = 10^j;
```

```
        save('objfun_mod3_exp_sigma0_Arrhenius.mat','t_exp1','D_exp1',...
            'Temp','Conc','H_seg','gamma_b0','sigma_0_c0','sigma_0_c1');
        x0 = [Q_L_c0 Q_L_c1];
        options = optimset('Display','off');
        xsol = fminsearch(@objfun_mod3_sigma0_Arrhenius,x0,options);

        disp(['xsol(1): ' num2str(xsol(1))])
        disp(['xsol(2): ' num2str(xsol(2))])

        Q_L_c0 = xsol(1);
        Q_L_c1 = xsol(2);

        disp(['f: ' num2str(objfun_mod3_sigma0_Arrhenius(xsol))])
        f = objfun_mod3_sigma0_Arrhenius(xsol);
        if f <= best
            a = Q_L_c0;
            b = Q_L_c1;
            best = f;
        end
    end
end

Q_L_c0 = a;
Q_L_c1 = b;

%% Optimization IV
% In this optimization, the previous solutions for the temperature
% dependent constants are used as starting points for the final
% optimization.  Without these different steps, the optimization may not
% converge to a valid solution.

save('objfun_mod4_exp_sigma0_Arrhenius.mat','t_exp1','D_exp1','Temp',...
    'Conc','H_seg','gamma_b0');
x0 = [sigma_0_c0 sigma_0_c1 Q_L_c0 Q_L_c1];

options = optimset('Display','off');
xsol = fminsearch(@objfun_mod4_sigma0_Arrhenius,x0,options);

disp(['xsol(1): ' num2str(xsol(1))])
disp(['xsol(2): ' num2str(xsol(2))])
disp(['xsol(3): ' num2str(xsol(3))])
disp(['xsol(4): ' num2str(xsol(4))])
```

```
sigma_0_c0 = xsol(1);
sigma_0_c1 = xsol(2);
Q_L_c0 = xsol(3);
Q_L_c1 = xsol(4);

disp(['f: ' num2str(objfun_mod4_sigma0_Arrhenius(xsol))])

% It is apparent from the value of `f' (goodness of fit) that the fit is
% not as good as individually fitting the model to each specific
% temperature/concentration combination.  But, the following fit better
% depicts the temperature dependence aspects than any of these individual
% fits.

%% Plot
% Plot the experimental results with the model results

x0 = [sigma_0_c0 sigma_0_c1 Q_L_c0 Q_L_c1];
hold on

% Plot the thermokinetic model curves
for i = 1:length(Temp)
    [t_a, D_t] = objfun_mod4_plot_sigma0_Arrhenius(x0,i);
    if i == 1
        h1 = plot([0 t_a], [D_exp1(1,i) D_t],'-r','LineWidth',3);
    elseif i == 2
        h2 = plot([0 t_a], [D_exp1(1,i) D_t],'-g','LineWidth',3);
    elseif i == 3
        h3 = plot([0 t_a], [D_exp1(1,i) D_t],'-c','LineWidth',3);
    elseif i == 4
        h4 = plot([0 t_a], [D_exp1(1,i) D_t],'-b','LineWidth',3);
    end
end

% Plot the experimental data
count = 0;
for i = 1:2:39
    x = num(:,i);
    y = num(:,i+1);
    imod = (i+1)/2;
    if inc(imod)
        count = count + 1;
        if count == 1
            h1 = plot(x,y,'or','MarkerSize',8,'MarkerFaceColor','r');
```

```
elseif count == 2
    h2 = plot(x,y,'og','MarkerSize',8,'MarkerFaceColor','g');
elseif count == 3
    h3 = plot(x,y,'sc','MarkerSize',8,'MarkerFaceColor','c');
elseif count == 4
    h4 = plot(x,y,'sb','MarkerSize',8,'MarkerFaceColor','b');
end
if count >= 1
    ylim([5 35])
    xlim([-100 6000])
    if i == 7
        ylim([0 600])
        legend([h1 h2 h3 h4],'nc Fe 400\circ{C}','nc Fe 500\circ{C}',...
            'nc Fe 600\circ{C}','nc Fe 700\circ{C}',...
            'Location',[0.76 0.81 0.01 0.01]);
    elseif i == 15
        legend([h1 h2 h3 h4],'nc Fe-0.5%Zr 700\circ{C}',...
            'nc Fe-0.5%Zr 800\circ{C}','nc Fe-0.5%Zr 900\circ{C}',...
            'nc Fe-0.5%Zr 1000\circ{C}',...
            'Location',[0.73 0.21 0.01 0.01]);
    elseif i == 23
        legend([h1 h2 h3 h4],'nc Fe-1%Zr 700\circ{C}',...
            'nc Fe-1%Zr 800\circ{C}','nc Fe-1%Zr 900\circ{C}',...
            'nc Fe-1%Zr 1000\circ{C}',...
            'Location',[0.73 0.21 0.01 0.01]);
    elseif i == 31
        legend([h1 h2 h3 h4],'nc Fe-4%Zr 700\circ{C}',...
            'nc Fe-4%Zr 800\circ{C}','nc Fe-4%Zr 900\circ{C}',...
            'nc Fe-4%Zr 1000\circ{C}',...
            'Location',[0.73 0.21 0.01 0.01]);
    elseif i == 39
        legend([h1 h2 h3 h4],'nc Fe-10%Zr 700\circ{C}',...
            'nc Fe-10%Zr 800\circ{C}','nc Fe-10%Zr 900\circ{C}',...
            'nc Fe-10%Zr 1000\circ{C}',...
            'Location',[0.73 0.21 0.01 0.01]);
    end
    legend('boxoff')
    xlabel('Time (s)',...
        'FontSize',30, 'FontName','Times', 'FontWeight','b');
    ylabel('Grain Size (nm)',...
        'FontSize',30, 'FontName','Times', 'FontWeight','b');
    set(gca, 'FontSize',24, 'FontName','Times', 'LineWidth',2,...
        'TickDir','out','XMinorTick','on','YMinorTick','on');
```

```
            set(get(gca,'Children'),'MarkerSize',8, 'LineWidth',2,...
                'MarkerEdgeColor','k')
            axis square
            xlabel(get(get(gca,'xlabel'),'String'), 'FontSize',30, ...
                'FontName','Times', 'FontWeight','b');
            ylabel(get(get(gca,'ylabel'),'String'), 'FontSize',30, ...
                'FontName','Times', 'FontWeight','b');
            set(gca, 'FontSize',24, 'FontName','Times', 'LineWidth',1);
            title('remove')
            legend('boxoff')
            axis square
            set(gcf,'Position',[1 1 1200 1200])
        end
    end
end
```

Appendix C. Thermokinetic Model Optimization Function MATLAB Script

---

This appendix appears in its original form, without editorial change.

```
%% Thermokinetic Grain Growth Model
% ---------------------------------
% Mark Tschopp, U.S. Army Research Laboratory, 2013-2014
% Email: mark.a.tschopp@us.army.mil
%
% The thermokinetic grain growth model is based on Reference [1] by Chen
% and colleagues.
%
% Reference:
% [1] Chen, Liu, Yang, Shen, Acta Materialia, 60 (2012) 4833.
%
% This is the optimization function used for the final optimization:

function [t_a, D_t] = objfun_mod4_plot_sigma0_Arrhenius(x,c)

sigma_0_c0 = x(1);
sigma_0_c1 = x(2);
Q_L_c0 = x(3);
Q_L_c1 = x(4);

R = 8.3145;             % J/mol K; ideal gas constant
V_m =  7.1/(100^3);     % m3 mol-1; Molar volume
M_0 = 0.8;              % m mol s-1 J-1; Interface mobility
D_D0 = 1;               % interface diffusion
D_L0 = 1;               % lattice diffusion

t_exp1 = []; D_exp1 = [];
load('objfun_mod4_exp_sigma0_Arrhenius.mat');

i = c;

T = Temp(i);
x_0 = Conc(i);
t_exp = t_exp1(:,i);
D_exp = D_exp1(:,i)';

sigma_0 = sigma_0_c0 + sigma_0_c1*T;
Q_L = Q_L_c0*exp(-sqrt(Q_L_c1^2)/(R*T));

sigma_1 = sigma_0 - gamma_b0*(R*T*(log(x_0))+H_seg);
sigma_2 = 3*gamma_b0^2*R*T*V_m/x_0;
Q_1 = Q_L + R*T*log(D_D0/D_L0)-sigma_0/gamma_b0 + (R*T*(log(x_0))+H_seg);
Q_2 = 3*R*T*V_m*gamma_b0/x_0;
```

```
D_star = -sigma_2/sigma_1;

clear t_a D_t
count = 0;

t_plot = t_exp;
D_0 = D_exp(1)*10^(-9);

for ti = 1:length(t_plot)
    t = t_plot(ti);

    count = count + 1;
    xTol = 0.001e-10;
    xLower = D_0;
    xUpper = D_star;
    LHS = 0.5*((xLower+sigma_2/sigma_1)^2-(D_0+sigma_2/sigma_1)^2)-...
    (Q_2/(R*T)+2*sigma_2/sigma_1)*(xLower-D_0)+...
    (sigma_2^2/sigma_1^2+sigma_2/sigma_1*Q_2/(R*T)+1/2*(Q_2/(R*T))^2)*...
    log((sigma_1*xLower+sigma_2)/(sigma_1*D_0+sigma_2)); %
    RHS = sigma_1*M_0*exp(-Q_1/(R*T))*t;
    diff_S = LHS-RHS;
    yLower = diff_S;

    xMid = (xLower + xUpper)/2.0;
    LHS = 0.5*((xMid+sigma_2/sigma_1)^2-(D_0+sigma_2/sigma_1)^2)-...
    (Q_2/(R*T)+2*sigma_2/sigma_1)*(xMid-D_0)+...
    (sigma_2^2/sigma_1^2+sigma_2/sigma_1*Q_2/(R*T)+1/2*(Q_2/(R*T))^2)*...
    log((sigma_1*xMid+sigma_2)/(sigma_1*D_0+sigma_2)); %
    RHS = sigma_1*M_0*exp(-Q_1/(R*T))*t;
    diff_S = LHS-RHS;
    yMid = diff_S;

    iters = 0;
    while (xUpper - xLower)/2.0 > xTol
        iters = iters + 1;
        if yLower * yMid > 0.0
            xLower = xMid;
        else
            xUpper = xMid;
        end
        xMid = (xLower + xUpper)/2.0;
        LHS = 0.5*((xMid+sigma_2/sigma_1)^2-(D_0+sigma_2/sigma_1)^2)-...
        (Q_2/(R*T)+2*sigma_2/sigma_1)*(xMid-D_0)+...
```

```
        (sigma_2^2/sigma_1^2+sigma_2/sigma_1*Q_2/(R*T)+1/2*(Q_2/(R*T))^2)*...
        log((sigma_1*xMid+sigma_2)/(sigma_1*D_0+sigma_2)); %
        RHS = sigma_1*M_0*exp(-Q_1/(R*T))*t;
        diff_S = LHS-RHS;
        yMid = diff_S;
    end

    if xMid > D_star, xMid = D_star; end
    t_a(count) = t;
    D_t(count) = xMid*10^9;

end
end
```

1 (PDF)	DEFENSE TECHNICAL INFORMATION CTR DTIC OCA
2 (PDF)	DIRECTOR US ARMY RESEARCH LAB RDRL CIO LL IMAL HRA MAIL & RECORDS MGMT
1 (PDF)	GOVT PRINTG OFC A MALHOTRA
29 (PDF)	RDRL WM B FORCH S KARNA J MCCAULEY RDRL WMM J BEATTY R DOWDING J ZABINSKI RDRL WMM D R BRENNAN R CARTER K CHO A GIRI B MCWILLIAMS RDRL WMM E J ADAMS J LASALVIA J SINGH J SWAB J SYNOWCZYNSKI DUNN RDRL WMM F B BUTLER J CHINELLA K DARLING K DOHERTY S GRENDAHL L KECSKES E KLIER H MAUPIN H MURDOCH T SANO M TSCHOPP RDRL WMM G J ANDZELM A RAWLETT